BOSTON UNIVERSITY
COLLEGE OF ENGINEERING

Dissertation

THE SPATIAL EXTENT OF POINT DEFECTS IN SILICON: EXPERIMENTS AND MODELING

by

ANURADHA MURTHY AGARWAL

M.Sc., Poona University, 1982
M.S., San Jose State University, 1985

Submitted in partial fulfillment of the
requirements for the degree of
Doctor of Philosophy
1994

Approved by

First Reader ______________________________

Scott T. Dunham, Ph.D.
Professor of Electrical Engineering

Second Reader ______________________________

Theodore D. Moustakas, Ph.D.
Professor of Electrical Engineering

Third Reader ______________________________

M. Selim Ünlü, Ph.D.
Professor of Electrical Engineering

ACKNOWLEDGEMENT

I would like to sincerely thank my advisor, Professor Scott T. Dunham, who has been in every way a friend, philosopher and guide to me during the entirety of my graduate work at Boston University. If I had to go through this degree one more time (which I thankfully don't!), I would pick him as my advisor all over again. I have benefitted tremendously from my association with him due to his fund of knowledge, keen insights, genuine interest and enthusiasm, not to mention the several enjoyable group outings he often spearheaded! I am indebted to Professor Theodore D. Moustakas for continually providing a motivating and inspiring environment in which to work. Also, I would like to thank Professor Selim Unlu for his expert and helpful comments during the last phase of my PhD. Many thanks are due to Prof. Mark Law from the University of Florida for making necessary modifications in the SUPREM IV simulation program which I used for all my modeling work.

None of my experimental work would have been possible if not for the excellent facilities at the Integrated Circuit Laboratory, Technology Research Laboratory and the Central Research Facility at MIT. I would like to thank Professors Martin Schmidt, Rafael Reif and Dmitri Anoniadis for allowing me access to these facilities. I would also like to thank the people affiliated with ICL and TRL who helped me in all my silicon processing needs, especially Octavio Hurtado, Joe Walsh, Paul McGrath, Paul Tierney, Nestore Polce, Brian Foley, Velma McClure and Linus Cordes. My thanks to An Lee at Boston University SEM facility. I am very grateful to SEMATECH for funding my research for the entire duration of my study of point defects in silicon.

A great deal of gratitude goes out to my friends and office-mates (past and present) who were there through thick and thin with their advice and enlightening discussions and with whose companionship Boston University came to mean home. This list includes (in the order in which I met them) Nanseng Jeng, Misako Matsuoka, Mitra Navi, Jim Huang, Nat Collins, Fred Wittel and Can Dong Wu. A heartfelt thanks goes to Nanseng Jeng and Nat Collins for paving the way for my simulation work with their software package SERAPES. A big thanks are also due to Nanseng Jeng and Fred Wittel, who helped me to maintain the tedious but important spreading resistance set-up at our laboratory.

I would also like to thank my several friends in California where I landed when I first arrived in this country and to the friends I have in the Boston area, all of whom motivated me to finish as soon as possible (without meaning to be so helpful) by never failing to ask me how much longer I had before I would graduate.

I owe a million thanks to all in my family and I dedicate this to my parents with the deepest of gratitude and love for always providing an appropriate learning environment and nurturing my interest in science. Finally, I owe a large chunk of my sanity to my husband, Anant, without whose constant encouragement I would never have seen the light at the end of the tunnel.

THE SPATIAL EXTENT OF POINT DEFECT INTERACTIONS IN SILICON: EXPERIMENTS AND MODELING

(Order No.)

ANURADHA M. AGARWAL
Boston University, College of Engineering, 1994
Major Professor: Scott T. Dunham, Professor of Electrical Engineering.

Abstract

Fabrication processes for devices in silicon frequently disturb the equilibrium concentration of point defects. These processes thus affect the diffusion of dopants which occur via point defect interactions. An understanding of the spatial extent of the interactions, typically spanning distances of up to tens of microns, is even more critical as device dimensions shrink to sub-micron regimes. Additionally, the determination of accurate point defect parameters, from models that include the spatial extent of point defect interactions, is essential to the development of fabrication process simulators. In this work, a physically sound model which includes important bulk and surface-film interactions that have been neglected in previous work [26] is presented. In particular, bulk Frenkel pair recombination is included, while at interfaces, segregation to films as well as surface regrowth are considered.

A series of experiments were performed to study the spatial extent of point defect influence. Most of our experiments are based on the extent of OED of phosphorus because the measurement of oxidation enhanced diffusion (OED) of phosphorus leads to an understanding of the silicon interstitial interactions as phosphorus diffuses predominantly via silicon interstitials. In the first series of experiments, we used buried phosphorus marker layers to reduce the effects of surface interactions while attempting to focus on the bulk effects. Additionally, to examine the effects of silicon material type on OED, we used four different types of silicon. Silicon membrane structures were formed, using backside anisotropic silicon etching, to study the effect

of the distance of point defect injection from the buried layers. The next series of experiments investigated the surface effects either by using phosphorus marker layers directly beneath a surface film or by a microscopic inspection of the silicon surface after long time and high temperature inert ambient anneals.

Finally, the validity of the model was tested using a broad range of data obtained both from this work as well as from literature sources. The experimental data was chosen to span conditions which had previously resulted in widely discrepant calculations of point defect parameters. The results indicate that a physically sound model which includes the spatial extent of point-defect interactions can fit a range of data using a single consistent set of point defect parameters, and can thereby be used to improve the prediction capabilities of fabrication process simulators.

Contents

List of Tables

List of Figures

Chapter 1

Introduction

The shrinking dimensions of present-day silicon integrated circuit devices necessitates accurate predictions from fabrication process simulators. In most applications, a process simulator based on a physically sound mathematical model is preferred to one relying solely on empirical models because the latter is not founded on a clear understanding of the process itself and therefore cannot account for the complex interactions inherent in any real fabrication process. The prediction capability of both physical and empirical models, however, are limited by the accuracy of the experimentally measured material parameters they use.

Point defects play a role in the specific problem of accurate junction depth prediction via a process simulator. During a thermal fabrication process, routinely used substitutional dopants in silicon, for instance, phosphorus, arsenic, boron and antimony, diffuse via point defects and this defect-mediated dopant diffusion in silicon ultimately determines the depth of a junction in a device. Thus to enable accurate junction depth prediction, we must provide the simulator both with correct models as well as accurate values of point-defect parameters as obtained from experiments.

The nature of bulk defects in silicon may vary depending on the technique used for growth, being different for floatzone (FZ), Czochralski (CZ) and epitaxial (epi) silicon. Interactions of point defects with an interface, in a surface-film or within the bulk can significantly alter the equilibrium defect concentrations. Therefore, a physical understanding of the underlying mechanisms involved during these interactions is imperative for dynamic modeling of the system.

The goal of this work is to evaluate the spatial extent of point defect interactions in silicon within the framework of a consistent model and subsequently to use the results of several experiments in conjunction with our model to extract point defect parameters.

Chapter 2 contains a brief introduction to point-defect theory relevant to this work, reviews the previous work and provides a motivation for the present study. An important part of the previous work is the calculation of the silicon interstitial diffusion coefficient. The silicon interstitial diffusivity, calculated from various types of experiments, varies over several orders of magnitude. Discrepancies in calculated parameters can be attributed to the fact that important physical interactions are neglected in the simple models that are used to calculate them. Chapter 3 discusses two of these often ignored physical interactions, bulk recombination and film segregation, and builds up to a model that includes these mechanisms.

The experiments that have been performed to study the spatial extent of point defect interactions are described in Chapters 4, 5, 6 and 7. Chapters 4 and 5 discuss experiments to measure the dependence of oxidation-induced interstitial supersaturation on depth into the wafer (distance from the oxidizing wafer surface), using buried dopant marker layers. Such experiments markedly reduce the effects of interactions at the the nonoxidizing surfaces. In contrast, Chapter 6 emphasizes surface interactions by using marker layers located close to the nonoxidizing interfaces. To better understand the interactions occuring during intrinsic gettering, Chapter 7 describes the high-temperature and inert-ambient annealing experiments performed. Chapter 8 contains a comparison of experimental data to our physically-based model and yields point defect parameters. Data from this work is used in conjunction with data from several other sources available in literature to obtain a *single consistent set* of parameters. Finally, Chapter 9 contains the conclusions and some recommendations for future work.

Chapter 2

Background and Motivation

This chapter provides an overview of the current understanding of point-defect theory relevant to the present research work. It gives a brief outline of the previous experiments done in related areas and some of the theoretical models presented to date. Section 2.1 contains a brief discussion of the nature of point defects followed by a discussion of equilibrium point-defect interactions in Section 2.2. Section 2.3 considers non-equilibrium point defect interactions starting with effects of thermal processing on equilibrium point defect concentrations in Section 2.3.1. Next, the bulk interaction of point defects with oxygen precipitates in Czochralski silicon substrates is considered in Sec 2.3.2 and the surface interactions of point defects with oxide and nitride films are described in Sec 2.3.3.

Equilibrium concentrations of point defects in silicon are small even at high temperatures making direct experimental observations of these defects quite difficult. Section 2.4 describes various relevant previous experiments and methods designed to measure point-defect parameters via dopant-diffusion, focussing on oxidation, nitridation and oxynitridation enhanced or retarded diffusion experiments.

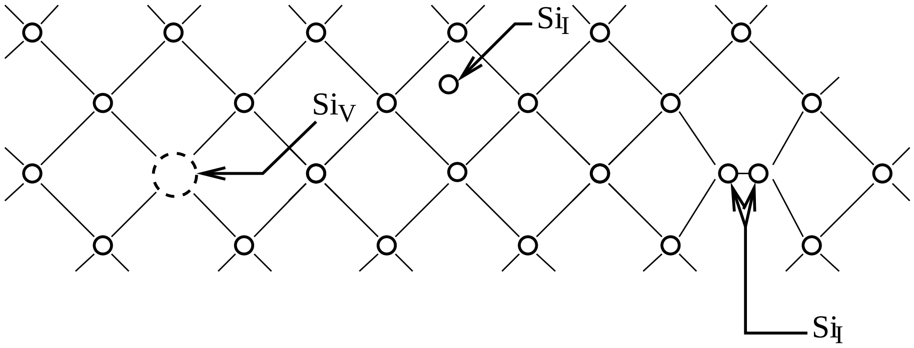

Figure 2.1: *Point Defects in Silicon: From left to right in the schematic are sketched a vacancy, an interstitial and an interstitialcy. Note that the same symbol is used for both an interstitial and an interstitialcy since they are currently indistinguishable from experiments.*

2.1 Nature of point defects

In a real undoped silicon crystal, the perfect lattice structure is interrupted by the presence of both point and extended defects. The former, which we focus on in this research, can be either impurity-related, which are formed when foreign impurities are introduced into the silicon lattice (often as substitutional dopants), or native point defects which can be classified broadly as interstitials, interstitialcies and vacancies. An interstitial, or more specifically in this case, a silicon self-interstitial, is an extra silicon atom located at a position other than a lattice site. An interstitialcy occurs when a region of silicon contains an extra silicon atom, and a vacancy, as the name suggests, is a lattice site without a silicon atom. Figure 2.1 shows schematic representations of each type of point defect. Since current dopant diffusion experiments are incapable of distinguishing between an interstitial and an interstitialcy, we shall use the word interstitial to mean either.

2.2 Equilibrium concentrations of point defects

For a temperature greater than absolute zero, in order for a crystal to minimize its free energy, thermodynamics predicts the existence of finite point-defect concentrations given by Swalin [79] and Lannoo and Bourgoin [51]

$$\frac{C_{\mathrm{X}}}{C_{\mathrm{S}}} = \theta_{\mathrm{X}} \exp\left[\frac{S_{\mathrm{X}}^{\mathrm{f}}}{k}\right] \exp\left[\frac{-H_{\mathrm{X}}^{\mathrm{f}}}{kT}\right], \tag{2.1}$$

where X is the point-defect species, C_{S} is the number of available lattice sites in the crystal, $H_{\mathrm{X}}^{\mathrm{f}}$ is the enthalpy of formation of X, $S_{\mathrm{X}}^{\mathrm{f}}$ is the formation entropy, and θ_{X} is the number of degrees of internal freedom of the defect on a site. Equilibrium concentrations of these defects depend on generation/recombination, both within the bulk of silicon as well as at surfaces. In dislocation-free silicon in equilibrium, the bulk generation/recombination mechanism is given by the Frenkel reaction,

$$I + V \leftrightarrow \phi, \tag{2.2}$$

where I is a silicon interstitial or interstitialcy and V is a silicon vacancy. The forward reaction represents the recombination mechanism while generation occurs when the reaction proceeds in the reverse direction, combining to approach equilibrium in the bulk. Another path towards equilibrium is generation/recombination in passive surface-films and at their interfaces with silicon. At such sites, interstitials and vacancies can be generated and annihilated independently of one another and this is given by the Schottky processes,

$$I + \text{surface} \leftrightarrow \text{surface}, \tag{2.3}$$

and

$$V + \text{surface} \leftrightarrow \text{surface}. \tag{2.4}$$

In the following discussion, a dilute concentration approximation is made whereby the point defects are considered unaffected by the presence of dopant atoms except indirectly by the change in Fermi level. These lattice point defects can be neutral, singly or multiply charged. The equilibrium neutral point-defect concentrations are independent of the Fermi level position. Neutral defects accept or donate electrons to become charged thus creating energy levels within the silicon band-gap which are either filled or empty depending on their position relative to the Fermi level. The total point-defect concentration includes the Fermi level independent neutral defects as well as the defects in various charge states. Thus, the Fermi level position, which is dependent on the doping level in silicon, determines the total equilibrium point-defect concentration. In our experiments therefore, we use low doping levels ($< 1\times10^{17}$ cm^{-3}) to ensure that intrinsic diffusion conditions are maintained at fabrication processing temperatures of 800°C to 1200°C. The added advantage is that these low concentrations of dopants also reduce the possibility of dopant-dopant interactions.

The migration of these species can occur either via diffusion or drift. For low doping levels of the ion implant used as a dopant marker layer, the Fermi level is almost spatially uniform at the temperatures for fabrication processing. Thus due to the absence of an electric field term we are able to ignore drift in this work and focus on diffusion which is dependent on the concentration gradient of point defects as given by Fick's laws. When recombination and generation terms are included in the equation, it takes on the form of the continuity equation, given as

$$\frac{\partial C_{\mathrm{X}}}{\partial t} = D_{\mathrm{X}} \frac{\partial^2 C_{\mathrm{X}}}{\partial x^2} - R + G \tag{2.5}$$

The time rate of change of point defect species is dependent on the spatial flux gradient which is the first term on the right side of the equation and includes the diffusion coefficient of the defect D_{X}, and on R and G, the bulk recombination and generation terms respectively.

2.3 Non-equilibrium concentrations of point defects

Concentrations of point defects can be altered under non-equilibrium conditions involving interactions with surface films or with bulk impurities. For example thermal oxidation injects interstitials, while thermal nitridation injects vacancies. Other processes that can affect the concentrations of point defects are oxygen precipitation in Czochralski silicon material and surface-film interactions of point defects, for example interactions with non-reacting oxide and nitride films and their interfaces with silicon. Inert ambient annealing of silicon wafers with thin surface oxides can significantly damage the wafer surfaces in addition to causing changes in point-defect concentrations.

2.3.1 Thermal fabrication processes

Thermal fabrication processes such as oxidation and nitridation affect the equilibrium concentration of point defects since they inject defects into the silicon substrate. As first pointed out by Hu [43], thermal oxidation of silicon injects self-interstitials into the bulk from the interface, causing an interstitial supersaturation. This is most often attributed to the fact that the volume per silicon atom in the oxide is about 2.2 times the volume per silicon atom in the silicon lattice. Expansion along the crystalline silicon surface cannot be accommodated due to lattice rigidity. Therefore, volume expansion occurs primarily in a direction perpendicular to the interface and excess silicon atoms are injected away from the interface as interstitials. Dopants that have oxidation enhanced diffusion profiles are said to display OED and those that show retarded diffusion profiles are said to display ORD.

A complementary process is the growth of a surface film of amorphous Si_3N_4 by thermal nitridation which causes a vacancy supersaturation. This has been explained by a vacancy injection or interstitial absorption mechanism from the surface, during the actual chemical reaction between the ambient and the silicon surface [25]. Dopants that have nitridation enhanced diffusion profiles are said to display NED while retarded profiles display NRD.

Thermal nitridation of an oxide film generates an interstitial supersaturation (or a vacancy undersaturation), which is explained by the fact that the nitride layer capping the slowly forming oxide is a good diffusion barrier, thereby driving the silicon interstitials generated, towards the bulk [25, 63]. Therefore, although the oxide thickness obtained by this technique is very small, the interstitial supersaturation caused here is much higher than during thermal oxidation of a bare silicon surface in which the interstitials can diffuse back into the growing oxide film as well as into the substrate. Dopants that have oxynitridation enhanced diffusion profiles are said to display ONED while oxynitridation retarded profiles display ONRD.

2.3.1.1 Interstitial injection via thermal oxidation

In our experimental work, we mainly use the OED of phosphorus as an indication of interstitial supersaturation because it diffuses predominantly via interstitials [27]. Interstitial supersaturation has been observed in many experiments, notably the quantitative measure of supersaturation during the thermal oxidation of silicon. Stacking fault growth during thermal oxidation has been observed experimentally since 1963 [88] and enhanced anomalous diffusion of boron in oxidizing ambients has been observed since 1969 [93]. However, in 1974, Hu [43] was the first one to point to the connection between the two effects by suggesting a model of interstitial injection at a surface that undergoes thermal oxidation. His model was based on the physical mechanism of interstitial formation during a somewhat incomplete oxidation giving rise to a generation rate of interstitials that is related linearly to the oxidation rate according to

$$\Delta C_{\mathrm{I}} \propto \frac{dx}{dt}. \tag{2.6}$$

The model was later corrected by Hu [44] to explain the non-linear dependence of interstitial injection on thermal oxidation by including a bimolecular reaction in which two silicon interstitials are used in each surface regrowth event. This led to a square root dependence,

$$\Delta C_{\mathrm{I}} \propto \sqrt{\frac{dx}{dt}}. \tag{2.7}$$

Several theories have since been proposed to explain quantitative links between thermal oxidation and interstitial supersaturation [89, 56, 28, 82, 21, 22, 17, 87]. In all cases, the general consensus is that a non-linear dependence exists between the excess interstitial generation and thermal oxidation rate, which over a limited range of oxidation rates can be approximated by:

$$\Delta C_{\mathrm{I}} \propto (\frac{dx}{dt})^n. \tag{2.8}$$

Since the studies of interstitial supersaturation during thermal oxidation are now quite well established, the study of point defect mediated oxidation enhanced diffusion of dopants is a desirable way in which to understand the various interactions of point defects in silicon.

2.3.2 Interactions with oxygen precipitates in the bulk

Intrinsic oxygen gettering is a standard process used in IC fabrication to help remove metal and other impurities to regions away from active device areas. This technique involves a three-step anneal process:

1. An initial high temperature step to outgas oxygen from the near surface active regions thereby decreasing the concentrations of oxygen interstitials in the surface areas

2. A low temperature nucleation step during which the oxygen interstitials react within the silicon substrate to form small oxygen precipitates (SiO_2)

3. A final high temperature growth step wherein the oxygen precipitates grow in size.

These precipitate sites act as gettering-centers, attracting metal impurities and trapping them. Thus, removal of gold impurities from active device regions, for instance, can increase the lifetime of minority carriers by reducing carrier recombination at gold trapping sites.

Since the precipitation process is akin to thermal oxidation, extra volume is necessary to accomodate the newly formed SiO_2 from the existing silicon,

$$\Omega = \frac{V_{\mathrm{ox}}}{V_{\mathrm{Si}}} \approx 2.2 \tag{2.9}$$

where V_{ox} is the volume per silicon atom in the oxide and V_{Si} is the volume in the silicon lattice. The suggested reaction mechanism of the intrinsic gettering step is given by Equation 2.10 [90],

$$(1+y)\mathrm{Si} + 2\mathrm{O_I} + y_1\mathrm{V_{Si}} \leftrightarrow \mathrm{SiO_2} \ + y_2\mathrm{Si_I} + \mathrm{stress}, \tag{2.10}$$

where the subscript I is used to denote the interstitial (either oxygen or silicon) and $y = y_1 + y_2$. Tan *et al.* [84] and Kennel *et al.* [48] suggest that the generation of silicon interstitials and the absorption of vacancies eliminate the need for any plastic deformation by providing the necessary volume.

In an attempt to test the oxygen precipitation reaction mechanism proposed in Equation 2.10, Tan *et al.* [84] and others have used a technique called FTIR (Fourier Transform Infrared Spectroscopy) which essentially involves a measurement of the IR absorption in the sample before and after a bulk oxygen precipitation reaction (i.e., intrinsic gettering). The heights of the absorption peaks for oxygen interstitials depend on their relative concentrations. A standard reference measurement is provided by a Floatzone (FZ) silicon sample because it lacks the high oxygen concentration of the Czochralski (CZ) wafer. Therefore, a direct comparison with a FZ wafer gives the absolute values of the interstitial oxygen concentrations before and after an intrinsic gettering step. Tan *et al.* focus on the bulk oxide precipitation process and hence do not perform the initial high temperature oxygen outgassing step which is useful only in denuding the active surface areas of oxygen. From their experimental observations Tan *et al.* postulated that the direction in which the reaction mechanism, Equation 2.10, proceeds, depends on the times and temperatures of both the low temperature pretreatments and the final anneal of their two-step oxygen precipitation process.

Observations of enhanced phosphorus diffusion in the silicon substrate during fast bulk oxygen precipitation [3, 49, 71] has been attributed to a supersaturation of interstitials during the precipitation process. Studies of the effect of surface films on the diffusion of phosphorus during the precipitation process are briefly discussed in Sec 2.3.3.

In summary, intrinsic gettering of Czochralski wafers converts the unstable interstitial oxygen atoms to a more stable SiO_2. This minimizes any uncontrolled silicon interstitial generation during later high temperature process sequences. Additionally, it removes metallic impurities from the device regions, thereby increasing minority carrier lifetimes.

2.3.3 Interactions with oxide and nitride films and their interfaces with silicon.

Thermal fabrication processes like oxidation, nitridation and chemical vapor deposition help in forming useful films on the silicon substrate. In the films, and at their interfaces with silicon, the presence of numerous sites for recombination allow vacancies and interstitials to annihilate independently of one another. The effect of oxide/nitride multilayers versus plain nitride caps on equilibrium interstitial concentrations in silicon substrates were investigated using either backside oxidation [3, 49, 72] or oxygen precipitation [71] as the source of interstitials. Rogers *et al.* [72, 71] measured the growth/shrinkage of stacking faults, Kennel *et al.* [49] monitored the actual oxygen precipitation process using FTIR spectroscopy while Ahn [3] measured enhanced dopant diffusion. All studies concluded that the Si-SiO_2 interface must have a higher recombination (annihilation) velocity for interstitials than the Si-Si_3N_4 interface. Details of one of Ahn's experiments to determine point defect parameters is discussed in Section 2.4.

As discussed in Sec 2.3.2, inert ambient annealing is an important processing step in VLSI fabrication technology as a part of the intrinsic gettering sequence for Czochralski silicon wafers. The effect of this step at high temperatures with only a thin oxide present on the silicon wafer has been shown by Ahn [3] to be a vacancy source (or interstitial sink), from his observations of enhanced diffusion of Sb and simultaneous retarded phosphorus diffusion during argon annealing for 8 hours at 1100°C. Additionally, such an anneal yields surface defects that are visible even under a simple optical microscope [40, 74, 38, 68, 70]. Pyramidal etch-pit structures similar to anisotropic solution etching was observed. This has been attributed by Yonehara *et al.* [80] and Tabe [81] to the reaction,

$$\mathrm{SiO_2 + Si \rightarrow 2SiO} \uparrow . \tag{2.11}$$

In the absence of a thin oxide at these high temperatures, the silicon is etched by the reaction mechanism proposed by Gelain *et al.* [30],

$$\mathrm{O_2 + 2Si \rightarrow 2SiO} \uparrow . \tag{2.12}$$

2.4 Measurement of point-defect parameters

Since native point defects in silicon are present in very small concentrations, especially at low temperatures, direct observation of vacancy or interstitial properties is difficult. Recently however, the positron annihilation experiment technique in silicon has begun to be applied to study native point defects in semiconductors [10, 14, 9, 11, 13]. Although vacancies were observed at temperatures greater than 1100°K via positron lifetime measurements [12], interstitials cannot be observed by this technique. Therefore, several indirect measurement techniques for point-defect parameters have been developed. For instance, the presence of vacancies and interstitials in silicon have been confirmed indirectly [27] through the study of dopant diffusion and silicon self-diffusion. Dopants in the semiconductor diffuse via point defects and provide a means to study point-defect parameters like diffusivity, equilibrium concentrations and interface recombination velocity.

Dopants can diffuse via interstitials or vacancies. The enhancement or retardation factor in dopant diffusion is calculated from

$$\frac{D_{\mathrm{A}}}{D_{\mathrm{A}}^{*}} = f_{\mathrm{AI}}\frac{C_{\mathrm{I}}}{C_{\mathrm{I}}^{*}} + (f_{\mathrm{AV}})\frac{C_{\mathrm{V}}}{C_{\mathrm{V}}^{*}}, \tag{2.13}$$

where D_{A} is the diffusion coefficient of the dopant "A" under investigation, D_{A}^{*} is its equilibrium value, f_{AI} is the fraction of dopant "A" diffusing via interstitials, (f_{AV}) is the fraction diffusing via vacancies, and C_{I} is the concentration of interstitials and C_{I}^{*}, its equilibrium value. Experiments that include thermal processes which inject interstitials, for instance the thermal oxidation or the thermal oxynitridation process, evidenced by stacking fault growth, show an enhanced phosphorus diffusion profile (OED or ONED), and a retarded antimony diffusion profile (ORD or ONRD).

In contrast, experiments including thermal processes which inject vacancies, for instance the thermal nitridation process, evidenced by stacking fault shrinkage, show a retarded phosphorus diffusion profile (NRD) and an enhanced antimony diffusion profile (NED). Arsenic shows small enhancement in both cases and boron behaves much like phosphorus.

From such data one can conclude that phosphorus diffuses predominantly via interstitials and antimony diffuses predominantly via vacancies [25, 24]. Other ex-

Table 2.1: *Dopant-fraction diffusing via interstitials at 1100°C.*

Dopant (A)	f_{AI}	Observation	References
Phosphorus	0.97	OED,NRD	[27]
Antimony	0.03	ONRD,ORD	[27]
Arsenic	0.40	ONED,NED	[27]
Boron	0.80	OED,NRD	[83, 27]

perimental evidence points to the fact that arsenic diffuses via both interstitials as well as vacancies and boron diffuses preferentially via interstitials. Table 2.1 gives an estimate of the interstitial component of diffusion for each of the dopants listed.

Thus in Equation 2.13, f_{AI} is almost unity for phosphorus and almost zero for antimony. We, therefore, use this knowledge about phosphorus to our advantage, by quantitatively measuring its diffusion profiles in oxidizing media versus inert media. The ratio of the two diffusivities thus obtained ($D_{\mathrm{P}}/D_{\mathrm{P}}^*$), approximates the interstitial supersaturation given by $C_{\mathrm{I}}/C_{\mathrm{I}}^*$.

A further assumption is that for long oxidation times, point-defect concentrations remain near local equilibrium due to I-V recombination [77]. This assumption is made based on observations of retarded diffusion of Sb in silicon [36] for short oxidation times and implies that we can use $C_{\mathrm{I}}C_{\mathrm{V}} \approx C_{\mathrm{I}}^*C_{\mathrm{V}}^*$.

In what follows, a brief review of relevant experiments performed to calculate point defect parameters is presented. Silicon self diffusion experiments have usually been carried out by monitoring the diffusion of radioactive silicon isotopes [27]. However, since the half-life of the only readily-obtainable silicon isotope (^{31}Si) is very small (2.6 hours), other techniques yielding similar information, like the use of Ge tracers, nuclear profiling and heavy metal diffusion [65, 78, 58], have also been investigated. The data obtained from these kinds of studies can yield information on the the temperature dependence of the products, $C_{\mathrm{I}}^*D_{\mathrm{I}}$ and $C_{\mathrm{V}}^*D_{\mathrm{V}}$. Commonly cited values are [83]:

$$C_{\mathrm{I}}^*D_{\mathrm{I}} = 3 \times 10^{25}\,\mathrm{cm}^{-1}\mathrm{sec}^{-1}\exp(-4.8\mathrm{eV}/\mathrm{kT}) \qquad (2.14)$$

$$C_{\rm V}^{*}D_{\rm V} \; = 2\times10^{22}\,{\rm cm^{-1}sec^{-1}}\exp(-4.0{\rm eV/kT}) \tag{2.15}$$

Using this $C_{\rm I}^{*}D_{\rm I}$ product and analyzing the time dependence of the gold gettering mechanism in silicon, Bronner *et al.* [6] estimated a value for $D_{\rm I}$ as,

$$D_{\rm I} \; = 600\exp(-2.44{\rm eV/kT}), \tag{2.16}$$

and for $C_{\rm I}$ as,

$$C_{\rm I} \; = 5\times10^{22}\exp(-2.36{\rm eV/kT}). \tag{2.17}$$

Most previous experiments in silicon used Czochralski silicon substrates, but because studies have shown that oxygen and carbon in silicon can disturb the equilibrium concentrations of point defects (as reviewed in Sec 2.3.2), floatzone silicon substrates are preferred instead.

2.4.1 Interstitial Diffusivity

Reported calculations of interstitial diffusivity vary over several orders of magnitude [4, 75, 85, 34, 33] as shown in Figure 2.2. This wide discrepancy is clearly unacceptable for reliable process predictions since most simulators numerically solve diffusion equations requiring the interstitial diffusion coefficient as a parameter.

Experiments of backside OED performed by Ahn *et al.* [3] used structures shown in the schematic of Figure 2.3. From the time dependence of the OED they concluded that interstitials take finite time to travel through the wafer thickness of 500μm. Using a standard model:

$$\frac{\partial C_{\rm I}}{\partial t} = D_{\rm I}^{\rm eff}\frac{\partial^2 C_{\rm I}}{\partial x^2} \tag{2.18}$$

$$D_{\rm I}\frac{\partial C}{\partial x} = \sigma_{\rm I}^{\rm eff}(C_{\rm I}-C_{\rm I}^{*}) \tag{2.19}$$

with a simple effective diffusivity accounting for all the bulk interactions and a constant recombination velocity at the surface constituting surface regrowth and other surface phenomena, they were able to calculate an *effective* diffusivity of $\approx 1\times10^{-9}$ cm^2/sec and an effective recombination velocity of $\approx 3\times10^{-7}$ cm/sec at 1100°C.

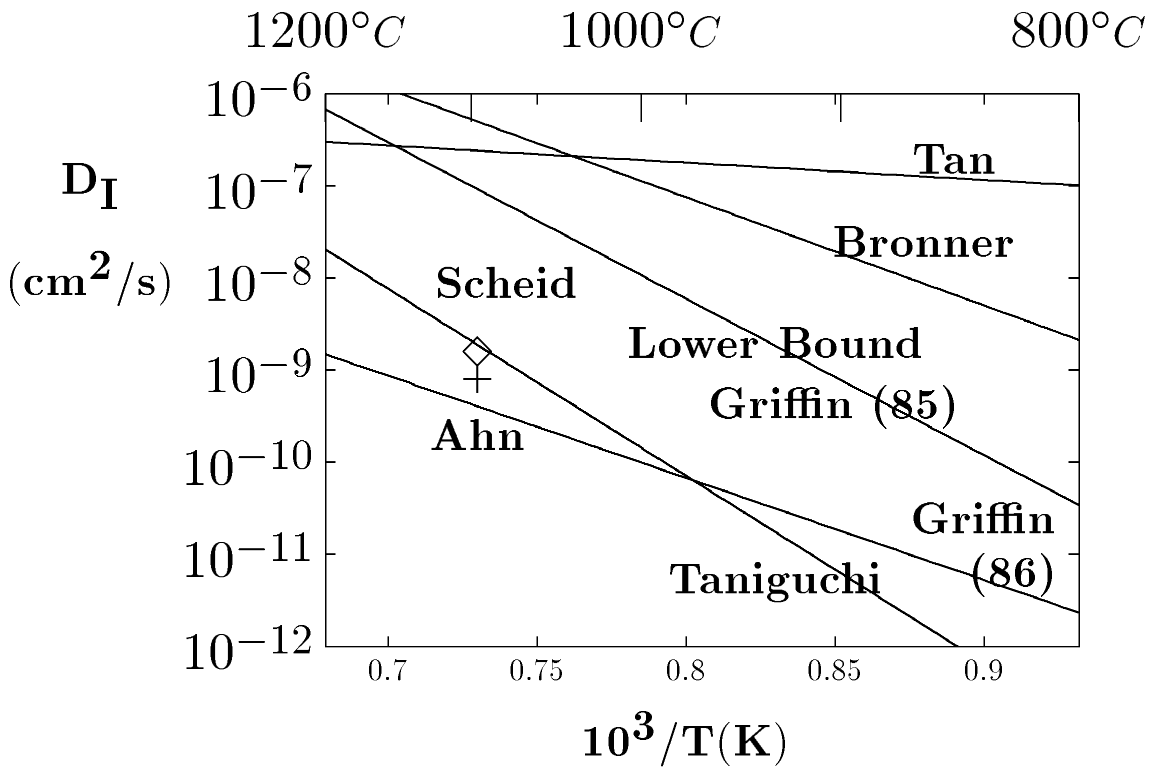

Figure 2.2: *Interstitial diffusivity as a function of temperature (from Griffin et al.)*

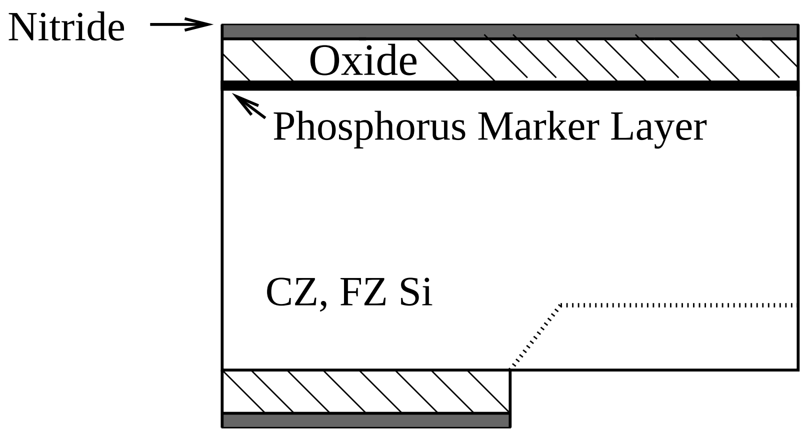

Figure 2.3: *Ahn et al.'s test structure of backside OED*

However, Ahn has observed that although the value of D_{I} he obtained was consistent with other stacking fault studies, it was much lower than the value obtained by Bronner *et al.* from gold gettering studies. He suggested that the true value of interstitial diffusivity can be high as calculated from metal gettering, but that the effective value that he calculated can appear reduced due to two reasons. The first reason is that the recombination of interstitials at the non-oxidizing oxide surface can be a time-dependent function that slowly decreases with time, thereby allowing a build-up in time at the frontside, during backside oxidation. The second reason is that bulk recombination of interstitials can slow down the diffusion front of interstitials and thus yield the observed time delay in build-up of interstitials at the frontside. Both of these interactions may explain the observed time-dependence in the OED, as well as the calculated lower effective interstitial diffusivity. Additionally, Ahn obtained the important result that the supersaturation at the oxidizing interface is independent of nearby sources and sinks and is entirely determined by the balance of the large generation and recombination fluxes at the oxidizing interface.

In later experiments, Griffin *et al.* [34] studied the lateral effects of OED by using a 2D test structure consisting of oxidizing regions separated by progressively narrower inert regions. Diffusion of a boron marker layer directly beneath the surface was monitored using junction staining techniques. Fig. 2.4 shows one such striped region with a measure of OED at the center of the inert region allowing a determination of the lateral extent of point defect influence. Griffin *et al.* modeled their experimental results and obtained a lateral decay length of interstitials as a function of time and temperature. Based on their modeling, they concluded that the steady-state values of decay length depended only on the ratio $D_{\mathrm{I}}/\sigma_{\mathrm{inert}}$, where σ_{inert} is the recombination velocity at the non-oxidizing inert interface, and the time characterizing the evolution of the lateral profile is determined by the ratio $D_{\mathrm{I}}/(\sigma_{\mathrm{inert}})^2$. By observing both of them, they were able to find unique values for each of these two point defect parameters. The standard model was adopted once again and effective values were calculated which were very similar to the ones previously calculated by Ahn *et al.* from their backside OED experiments. Griffin *et al.* also performed a very interesting experiment using a buried dopant marker layer. By using different thicknesses of the

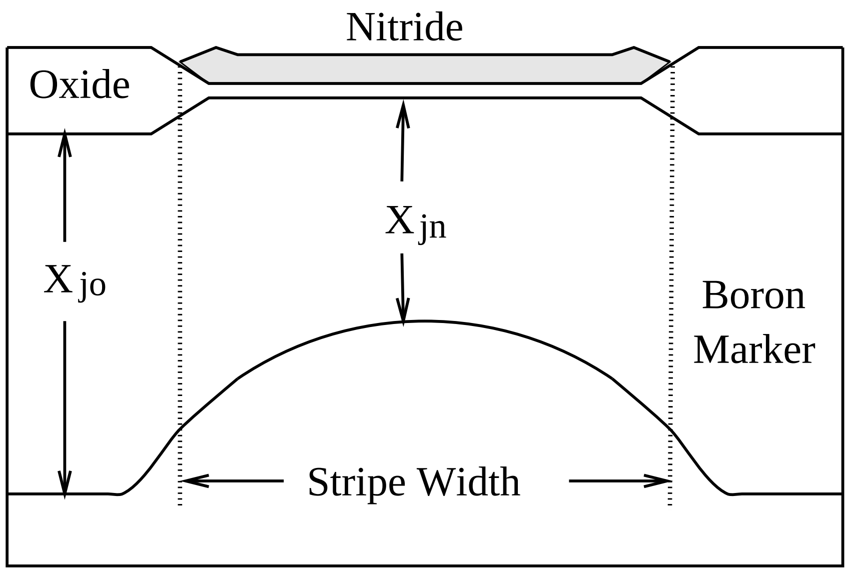

Figure 2.4: *Griffin et al.'s test structure for measuring the lateral extent of OED*

epitaxial film beneath which the dopant marker is located, they were able to inject interstitials, via thermal oxidation, at various distances from the buried dopant layer. If interstitials diffused slowly they expected to see greater OED beneath a 10μm film compared to a 40μm film. However, no such effect was observed after a 200 min. wet oxidation. Griffin *et al.* therefore suggested that true interstitial diffusivity can be high but there may be some trapping mechanism in floatzone and Czochralski substrates, absent in epitaxial silicon, which manage to slow down the interstitial front. The trapping mechanism can give rise to a slow effective diffusivity calculated from Griffin's lateral OED experiments and from Ahn's backside OED experiments. This was a significant step towards realizing that interactions of point defects in the bulk are important, although no trap candidate was suggested.

From the observation of almost unchanged OED under progressively narrower oxidizing stripes, Griffin *et al.* confirmed the conclusion from Ahn *et al.* that the oxidizing surface pinned the value of supersaturation from a balance of the large generation and recombination fluxes. The diffusion flux played no major role, again, since the presence of sources and sinks seemed not to affect the value of the supersaturation. Another important conclusion from Griffin's work was that the recombination flux at the oxidizing interface must be time-dependent because there cannot

Table 2.2: *Summary of previous calculations of effective interstitial diffusivity*

Type of experiment	Diffusion Through	Marker Location	Injection Level	Effective D_{I}	References
Backside Oxidation Lateral Extent of OED	CZ, FZ	Interface	Low	Low	[4, 75, 85] [34, 62]
Buried Layer	Epitaxial	Bulk	Low	High	[33]
Metal Gettering	CZ, FZ	Bulk	High	High	[5, 83]

be a step change in the recombination velocity at the transition region between the oxidizing and inert regions. Other studies of the lateral extent of point defect interactions were performed by Lin *et al.* [57] and Taniguchi *et al.* [86] who found short lateral diffusion lengths under pad-oxides. Another study of the effect of surface layers on point defect interactions was performed by Rogers *et al.* [72] who examined the growth/shrinkage of stacking faults beneath thermally grown oxides and CVD nitrides after backside oxidation and found that a model based on a time-dependent ratio of $\sigma_{\mathrm{I}}/D_{\mathrm{I}}$ produced a better fit to their data than a static model. This indicates that issues relating to interface interactions of point defects must be addressed.

Recently, Shibata *et al.* [76] have shown that when the oxidizing stripes are made very narrow (less than 2μm), the effects of the neighbouring surface sinks seem to affect the OED beneath the oxidized regions indicating that lateral point defect interactions are becoming increasingly important as dimensions continue to shrink in ULSI devices.

In summary, despite the large range of calculated values for interstitial diffusivity, individual experiments or types of experiments generally give consistent results. Table 2.2 summarizes these results. The results and models in the first two types of experiments yield a slow effective diffusivity value ($\approx 1\times10^{-9}$ cm^2/ sec), whereas the metal gettering experiments give a higher effective diffusivity ($\approx 1\times10^{-7}$ cm^2/sec).

Griffin *et al.* [32] explained these differences by assuming that trap species present in Czochralski and float-zone silicon, but absent from epitaxial silicon, slow down the propagating diffusion front of interstitials, thus resulting in a reduced effective diffusion coefficient. The fast diffusion noted in the metal gettering experiment is explained by assuming that the gettering process causes a much higher supersaturation of interstitials which rapidly fill the traps and allow unimpeded diffusion. One of the problems of this trapping model is that, to date, no plausible trap candidate present in floatzone but absent in epitaxial material, has been suggested.

An observation from Table 2.2 is that when defects are monitored near interfaces, as in Griffin *et al.*'s experiments of lateral OED and Ahn's OED in backside membrane structures, lower values of effective diffusivity are calculated. Standard models used in such calculations typically follow an over-simplified approach, for example, a simple effective diffusivity to account for all the bulk interactions and a constant recombination velocity at the surface to account for surface regrowth or film segregation, as given by Equations 2.18 and 2.19. However, an alternative explanation is that film-surface interactions play an important role and must be included in the models, not simply as a constant effective recombination (regrowth) velocity, but instead as a possible time-dependent parameter [72].

In the following chapter, as a result of the experimental information available in literature stressing the need to consider physical and spatial interactions, we present a mathematical model including bulk recombination of interstitials with vacancies, segregation of interstitials to surface oxide films and recombination of interstitials at interfaces.

Chapter 3

Consistent Model Including Physical Interactions

The previous chapter provided the motivation for developing a model that includes both bulk and surface interactions. In this chapter, we discuss important point defect interactions, specifically those of silicon interstitials.

Figure 3 is a schematic showing some of the point defect interactions in silicon. Interstitials (vacancies) can be injected at the surface during fabrication processing, for example, during thermal oxidation (thermal nitridation). These injected interstitials can recombine in the bulk or interact with extended defects like bulk oxygen precipitates or stacking faults. The salient point defect interactions considered in this work that have previously been largely ignored are bulk recombination and interactions with films with a non-constant recombination velocity, specifically, segregation of interstitials to surface films. Bulk recombination with vacancies slow down the diffusion front of interstitials giving a slower calculated effective value for diffusivity, while segregation of interstitials to films results in an effective recombination velocity which decreases with time, again appearing as a slower effective diffusivity when monitoring concentrations near substrate/film interfaces [18]. Table 2.2 suggests that film segregation interactions are particularly important, since the one experimental feature which predicts whether high or low diffusivity values will be calculated is

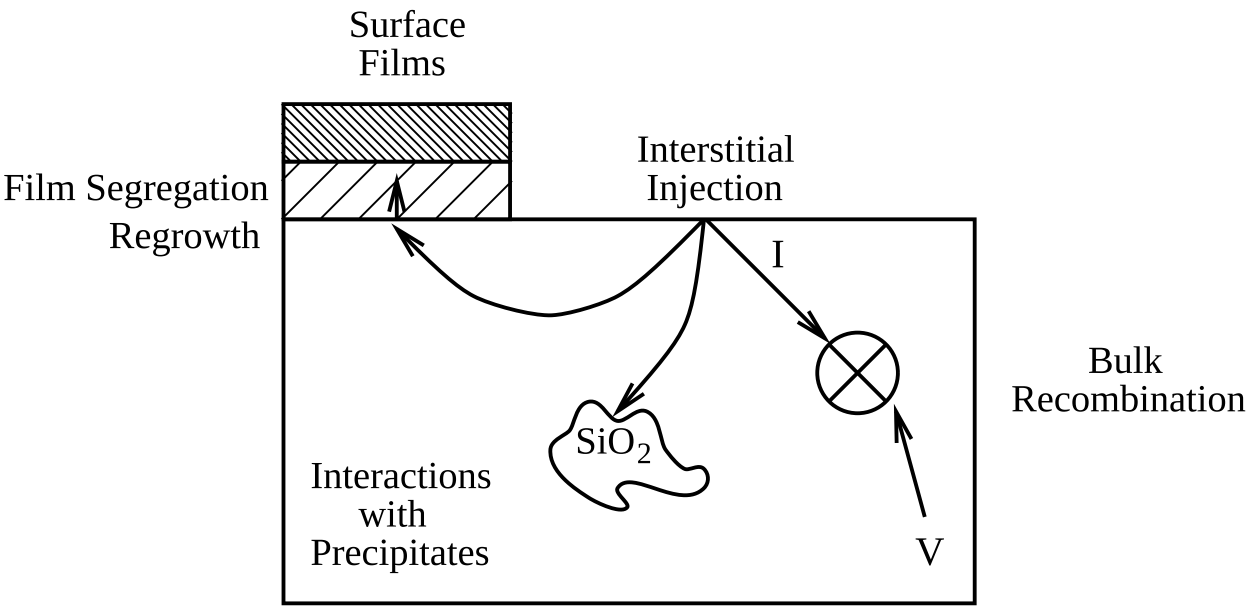

Figure 3.1: *Schematic showing bulk and surface interactions of point defects*

whether the interstitial concentration is monitored near an interface or within the bulk.

3.1 Bulk Recombination

To include the effect of interstitials being slowed by bulk recombination, we solve the continuity equations in the bulk, including Frenkel pair recombination:

$$\frac{\partial C_{\mathrm{I}}}{\partial t} = D_{\mathrm{I}} \frac{\partial^2 C_{\mathrm{I}}}{\partial x^2} - k_r (C_{\mathrm{I}} C_{\mathrm{V}} - C_{\mathrm{I}}^* C_{\mathrm{V}}^*) \tag{3.1}$$

$$\frac{\partial C_{\mathrm{V}}}{\partial t} = D_V \frac{\partial^2 C_{\mathrm{V}}}{\partial x^2} - k_r (C_{\mathrm{I}} C_{\mathrm{V}} - C_{\mathrm{I}}^* C_{\mathrm{V}}^*). \tag{3.2}$$

The boundary conditions correspond to point defect fluxes at growing oxide films and at nonoxidizing oxide films. At non-oxidizing SiO_2 film interfaces, we include a constant interface regrowth velocity which is proportional to the excess point defect concentration for each case as given by the Schottky reactions:

$$D_{\mathrm{I}} \frac{\partial C_{\mathrm{I}}}{\partial x} = \sigma_{\mathrm{I}} (C_{\mathrm{I}} - C_{\mathrm{I}}^*) \tag{3.3}$$

$$D_{\mathrm{I}} \frac{\partial C_{\mathrm{V}}}{\partial x} = \sigma_{\mathrm{V}} (C_{\mathrm{V}} - C_{\mathrm{V}}^*) \tag{3.4}$$

At the oxidizing Si/SiO_2 interface, interstitial generation and recombination is determined either from oxidation kinetics along with the known dependence of interstitial supersaturation on oxidation rate, or from available data at the oxidizing interface.

We use the SUPREM IV process simulator [52] to solve the coupled point defect equations given by Equations 3.1 and 3.2. The solution to this coupled system of equations together with its boundary conditions yields the interstitial supersaturation which we then compare to various data, both our own and that obtained from sources in the literature.

Several parameter choices exist for optimizing the fit of experimental data to the numerical simulations. To help identify the important parameters for these simulations, we begin by simple algebraic manipulations and re-arrangement of the continuity equations. Dividing each of the point defect diffusion equations by the product $C_{\mathrm{I}}^{*}C_{\mathrm{V}}^{*}$ and simplifying algebraically leads to:

$$\frac{\partial(C_{\mathrm{I}}/C_{\mathrm{I}}^{*})}{\partial t} = D_{\mathrm{I}}\frac{\partial^2(C_{\mathrm{I}}/C_{\mathrm{I}}^{*})}{\partial x^2} - k_r C_{\mathrm{V}}^{*}((C_{\mathrm{I}}C_{\mathrm{V}}/C_{\mathrm{I}}^{*}C_{\mathrm{V}}^{*}) - 1) \tag{3.5}$$

$$\frac{\partial(C_{\mathrm{V}}/C_{\mathrm{V}}^{*})}{\partial t} = D_{\mathrm{V}}\frac{\partial^2(C_{\mathrm{V}}/C_{\mathrm{V}}^{*})}{\partial x^2} - k_r C_{\mathrm{I}}^{*}((C_{\mathrm{I}}C_{\mathrm{V}}/C_{\mathrm{I}}^{*}C_{\mathrm{V}}^{*}) - 1). \tag{3.6}$$

Next, multiplying and dividing by C_{I}^{*} in the second term on the RHS of Equation 3.5 yields,

$$\frac{\partial(C_{\mathrm{I}}/C_{\mathrm{I}}^{*})}{\partial t} = D_{\mathrm{I}}\frac{\partial^2(C_{\mathrm{I}}/C_{\mathrm{I}}^{*})}{\partial x^2} - (k_r C_{\mathrm{I}}^{*})(\frac{C_{\mathrm{V}}^{*}}{C_{\mathrm{I}}^{*}}((C_{\mathrm{I}}C_{\mathrm{V}}/C_{\mathrm{I}}^{*}C_{\mathrm{V}}^{*}) - 1), \tag{3.7}$$

and together with Equations 3.3, 3.4 and 3.6, which are unchanged, a minimal set of parameters emerge. Since point defect supersaturations control dopant diffusion changes (Equation 2.13), a possible parameter set is D_{I}, $\mathrm{k}_r C_{\mathrm{I}}^{*}$, $C_{\mathrm{V}}^{*}/C_{\mathrm{I}}^{*}$, D_{V}, σ_{I} and σ_{V}. If we assume that the bulk recombination coefficient k_r is diffusion-limited [27], then

$$k_r = 4\pi a(D_{\mathrm{I}} + D_{\mathrm{V}}) \approx 4\pi a D_{\mathrm{I}} \approx 10^{-14}. \tag{3.8}$$

$D_{\mathrm{I}} \gg D_{\mathrm{V}}$ [27, 92], and thus the parameter $\mathrm{k}_r C_{\mathrm{I}}^{*}$ can be calculated from the $C_{\mathrm{I}}^{*}D_{\mathrm{I}}$ product, which we obtain from silicon self-diffusion data [83] as described in Equation 2.14. Furthermore, the $C_{\mathrm{V}}^{*}D_{\mathrm{V}}$ product, again obtained from silicon self-diffusion data [83] (Equation 2.15), allows us to calculate D_{V} given $C_{\mathrm{V}}^{*}/C_{\mathrm{I}}^{*}$ and D_{I}, where we use a fast interstitial diffusivity as obtained from metal gettering experiments [6], in keeping with our belief that the true value of interstitial diffusivity is high but is slowed due to bulk and surface-film interactions. Thus the parameter choices now reduce to C_V^*/C_I^*, σ_I and σ_V. We can examine their importance by changing their values in the numerical simulation and observing the corresponding change in supersaturation. The results are shown in Section 3.3.

3.2 Segregation to Surface Films

Interactions of point defects at nonoxidizing Si/SiO_2 interfaces can be more complicated than a simple constant recombination velocity. As discussed previously by Dunham [18], extension of models for the effect of oxidation on point defects to nonoxidizing films leads naturally to the conclusion that excess silicon can segregate to oxide films from the silicon and diffuse within that film. The importance of this process is supported by Ahn's observation of retarded diffusion of phosphorus and the simultaneous enhanced diffusion of antimony during inert ambient annealing and also by Fahey's and Griffin's calculations requiring a much higher effective recombination velocity at a nitrided oxide compared to a nitride-capped oxide. Figure 3.2 shows a schematic of the sequence of events beginning with interstitial injection from an oxidizing silicon interface followed by diffusion to the non-oxidizing Si/SiO_2 backside interface through the silicon. When there is a supersaturation of interstitials in the substrate, segregation of excess interstitials from the silicon sets up a diffusion gradient within the SiO_2 from the Si/SiO_2 interface to the SiO_2/Si_3N_4 interface. The latter interface is modeled as a reflecting boundary [17] owing to experimental observations showing Si_3N_4 as a diffusion barrier [61, 26]. This generates a flux of interstitials into the nonoxidizing SiO_2, with a decreasing gradient over time leading in turn to a flux into the film that decreases in time. The net result is an effective recombination velocity which decreases with time. Figure 3.3 shows a close-up view of the segregation mechanism at the non-oxidizing SiO_2 interface. In 2D lateral OED experiments, the non-oxidizing oxide film is adjacent to the oxidizing oxide film. Thus segregation and subsequent diffusion occurs laterally and the time-dependence effects are more pronounced as discussed further in Chapter 8.

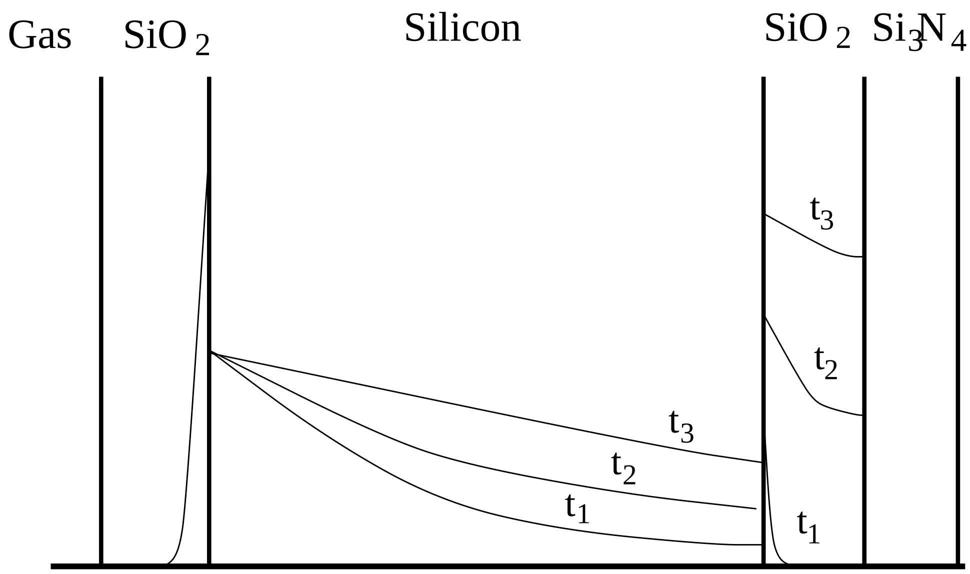

Figure 3.2: *Schematic of diffusion of interstitials from a growing* Si/SiO_2 *film interface to the inert oxide interface, followed by a subsequent segregation into the inert oxide and diffusion therein, for three different times, with* $t_1 < t_2 < t_3$.

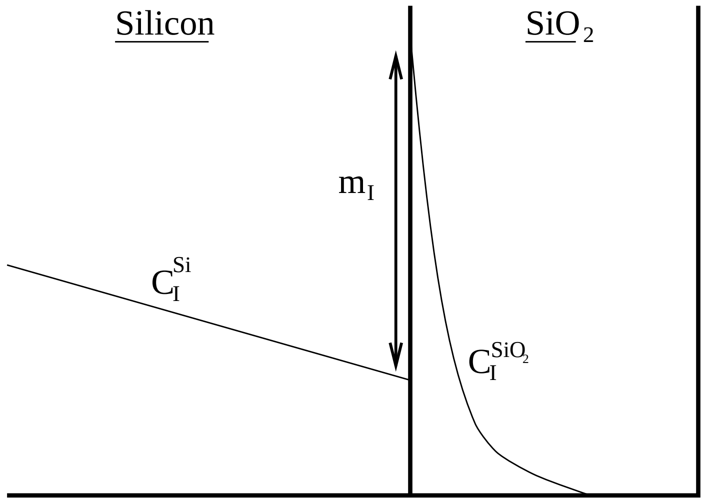

Figure 3.3: *Close-up view at the non-oxidizing* Si/SiO_2 *interface showing the segregation mechanism.* m_{Si/SiO_2} *is defined as the interstitial segregation coefficient.*

In our model, interstitials (or excess silicon) are assumed to segregate between the silicon and oxide with

$$C_{\mathrm{I}}^{\mathrm{SiO_2}}(0^+) = m_{\mathrm{Si/SiO_2}} C_{\mathrm{I}}^{\mathrm{Si}}(0^-), \tag{3.9}$$

where $m_{\mathrm{Si/SiO_2}}$ is defined as the interstitial segregation coefficient. The continuity equations in the silicon are given by Equations 3.1 and 3.2, but in addition we must include a continuity equation for interstitials within the oxide, given by

$$\frac{\partial C_{\mathrm{I}}^{\mathrm{SiO_2}}}{\partial t} = D_{\mathrm{I}}^{\mathrm{SiO_2}} \frac{\partial^2 C_{\mathrm{I}}^{\mathrm{SiO_2}}}{\partial x^2}. \tag{3.10}$$

The boundary conditions at the $\mathrm{Si/SiO_2}$ interface are given by

$$D_{\mathrm{I}}^{\mathrm{Si}} \frac{\partial C_{\mathrm{I}}^{\mathrm{Si}}}{\partial x}\bigg|_{\mathrm{Si/SiO_2}} = D_{\mathrm{I}}^{\mathrm{SiO_2}} \frac{\partial C_{\mathrm{I}}^{\mathrm{SiO_2}}}{\partial x} + \sigma_{\mathrm{I}}(C_{\mathrm{I}}^{\mathrm{Si}} - C_{\mathrm{I}}^{\mathrm{Si*}}), \tag{3.11}$$

and Equation 3.4. The $\mathrm{SiO_2/Si_3N_4}$ interface is assumed to be a reflecting boundary, so:

$$\frac{\partial C_{\mathrm{I}}^{\mathrm{SiO_2}}}{\partial x}\bigg|_{\mathrm{SiO_2/Si_3N_4}} = 0 \tag{3.12}$$

and

$$\frac{\partial C_{\mathrm{V}}{}^{\mathrm{SiO_2}}}{\partial x}\bigg|_{\mathrm{SiO_2/Si_3N_4}} = 0. \tag{3.13}$$

The initial conditions are given by,

$$C_{\mathrm{I}}(t=0) = C_{\mathrm{I}}^{\mathrm{Si*}} \tag{3.14}$$

and

$$C_{\mathrm{V}}(t=0) = C_{\mathrm{V}}^{\mathrm{Si*}}. \tag{3.15}$$

The interstitial diffusivity in the $\mathrm{SiO_2}$, $D_{\mathrm{I}}^{\mathrm{SiO_2}}$, is calculated from experiments involving the thermo-migration of dopants within the $\mathrm{SiO_2}$ [7]. Extrapolating from Celler *et al.*'s data, given by an Arrhenius relationship,

$$D_{\mathrm{I}}^{\mathrm{SiO_2}} = 13\,\mathrm{cm^2\ sec^{-1}} \exp(-4.5\mathrm{eV/kT}), \tag{3.16}$$

we obtain a diffusion coefficient for interstitials within the oxide to be approximately $4 \times 10^{-16}\mathrm{cm^2/sec}$ at 1100°C. To remain consistent with other experimental observations, we only allow as fitting parameters those that are not specified based on

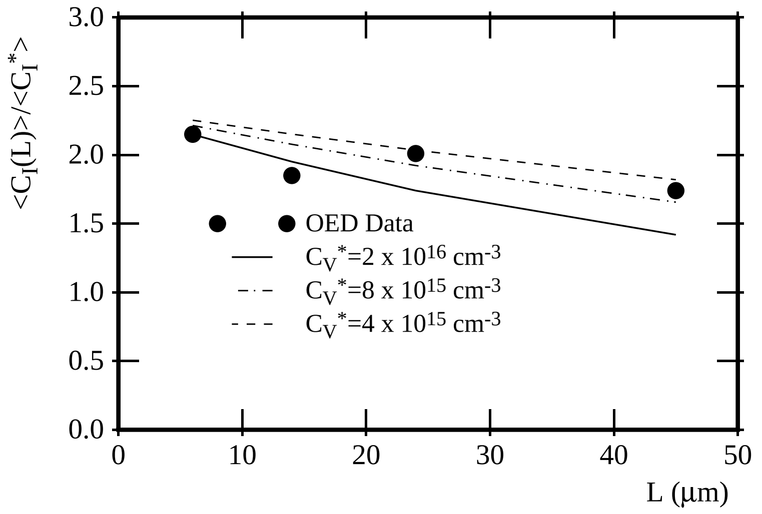

Figure 3.4: *The effect of varying C^*_{V} in the SUPREM IV diffusion solver for the example of frontside oxidation of an epitaxial film in dry* O_2 *for 1 hour at 1100°C as part of our buried layer membrane experiment.*

experiments reported in the literature. Thus, including the process of segregation of interstitials in our model, we obtain one additional fitting parameter which is the segregation coefficient, m_{I}. Section 3.3 contains the results of the numerical simulations designed to show the relevance of these parameters.

3.3 Simulation Results

Experiments from literature and from our own work have been simulated using SUPREM IV. The version of SUPREM IV that we use has been modified to allow segregation of interstitials to the inert oxide film and diffusion within the oxide. We change one parameter at a time while keeping the rest of the parameters fixed for the duration of that simulation. Figure 3.4 shows the effect of varying C^*_{V} in our frontside-oxidized, buried layer experiment which included a dry oxidation step for 60 mins at 1100°C for four different membrane thicknesses. The slope of the simulated curve increases as C^*_{V} is increased, reflecting greater bulk recombination of interstitials and hence a faster drop-off in the supersaturation with depth.

The effect of varying the bulk recombination coefficient k_r is shown in Figure 3.5.

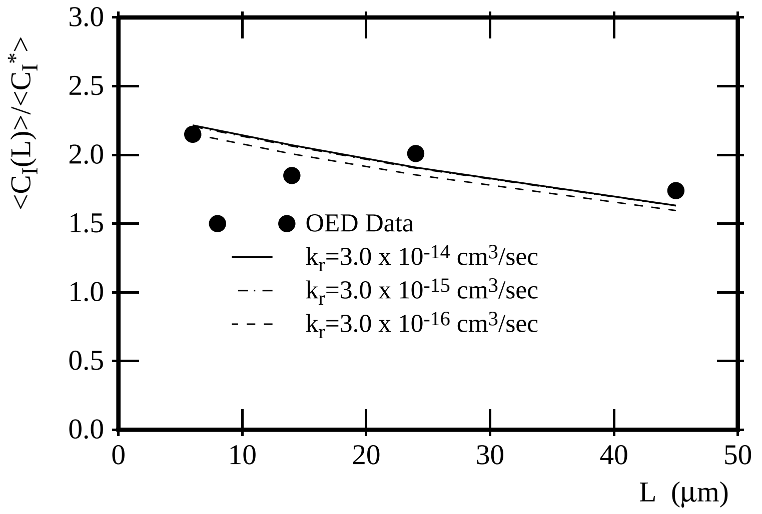

Figure 3.5: *The effect of varying k_r in the SUPREM IV diffusion solver for the example of frontside oxidation of an epitaxial film in dry* O_2 *for 1 hour at 1100°*C *as part of our buried layer membrane experiment.*

When the SUPREM IV default value for k_r at 1100°C is decreased by an order of magnitude, from 3×10^{-15}cm^3 sec^{-1} [36] to 3×10^{-16}cm^3 sec^{-1}, there is only a small reduction observed in calculated supersaturation. Similarly, when the recombination coefficient is increased by an order of magnitude from 3×10^{-15}cm^3 sec^{-1} [36] to 3×10^{-14}cm^3 sec^{-1}, in keeping with the diffusion-limited value (Equation 3.8), there is no change in calculated supersaturation and thus the effect of this parameter can be considered negligible. This low sensitivity of supersaturation on k_r, especially for high values, is attributed to the experimentally observed fast recombination obtained from Guerrero *et al.*'s [36] study of the retarded diffusion of antimony that keeps $C_{\mathrm{I}}C_{\mathrm{V}}$ near its equilibrium value of $C_{\mathrm{I}}^*C_{\mathrm{V}}^*$. Requirements for the choice of this parameter are then that it be consistent with the diffusion-limited value as well as satisfy the fast recombination observed. In our simulations, reported here and in Chapter 8, we therefore use the literature value from Guerrero *et al.* which is $k_r = 3\times10^{-15}$cm^3 sec^{-1} at 1100°C, in keeping with the above two requirements.

In Figure 3.6, the value of the regrowth velocity at the non-oxidizing oxide interface is varied for the case of backside oxidation using membrane structures in dry O_2 for 20 hours at 1100°C. As σ_{I} is decreased beyond $\approx 5\times10^{-5}$ cm/sec we see

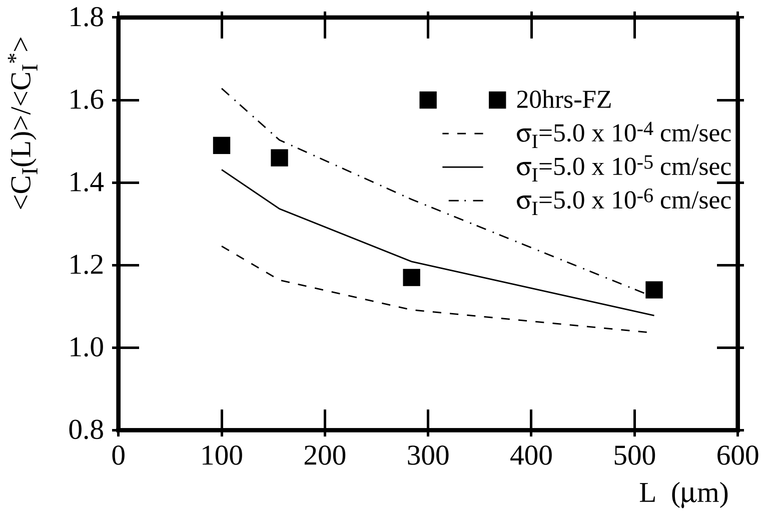

Figure 3.6: *The effect of varying $\sigma_{\rm I}$ in the SUPREM IV diffusion solver for the example of oxidation of backside membrane structures in floatzone silicon for 20 hours in dry* O_2 *at 1100°C, in our buried layer experiment.*

that there is relatively little effect on the value of supersaturation for all membrane thicknesses studied, possibly due to the fact that bulk recombination dominates as an interstitial sink at such low levels of interface recombination. However, an increased value for $\sigma_{\rm I}$ decreases supersaturation. This is as expected since now interface recombination and bulk recombination are comparable sinks. The largest effect is for thinnest membranes and can be intuitively explained by the small distance between the injecting interface and the recombining interface.

Figure 3.7 displays the effect of varying the vacancy recombination velocity at the Si/SiO$_2$ interface. Although a large effect can be seen by changing $\sigma_{\rm V}$ to a value several orders of magnitude larger than $1{\times}10^{-7}$, there is no difference seen when the parameter is further lowered, even to the limiting case of zero. The simulation clearly indicates that as the interface recombination velocity for vacancies increases, the supersaturation, especially for the thinnest membranes, falls off. Since surface recombination of both interstitials and vacancies have the same effect on interstitial supersaturation (Figures 3.7 and 3.6), we can reduce the number of parameters. Using the continuity equations for point defects together with their boundary conditions (Equations 3.1, 3.2, 3.3 and 3.4) and including the condition for fast recombination,

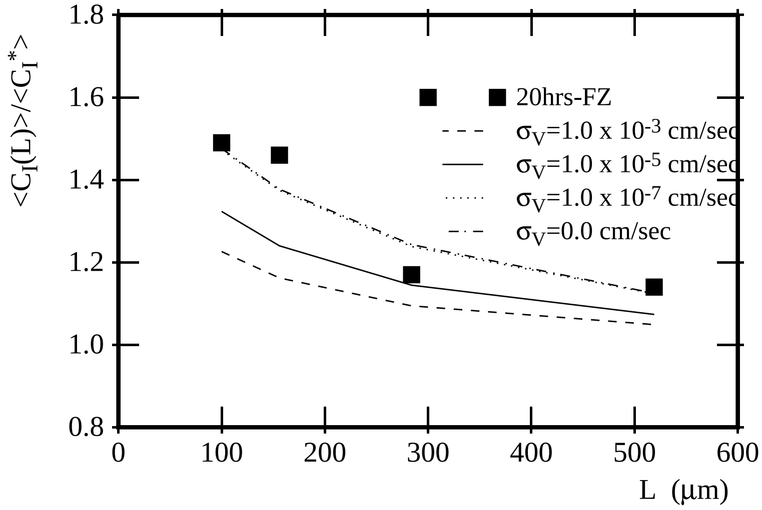

Figure 3.7: *The effect of varying* $\sigma_{\rm V}$ *in the SUPREM IV diffusion solver for the example of oxidation of backside membrane structures in floatzone silicon for 20 hours in dry* O_2 *at 1100°C, in our buried layer experiment.*

$C_{\rm I}C_{\rm V}\approx C_{\rm I}^*C_{\rm V}^*$, we obtain an effective interstitial recombination velocity, $\sigma_{\rm I}^{eff}$, which includes the effects of interstitial and vacancy recombination:

$$\sigma_{\rm I}^{eff} = \sigma_{\rm I} + \sigma_{\rm V}(\frac{C_{\rm V}^*}{C_{\rm I}}). \tag{3.17}$$

We use a constant value for $\sigma_{\rm I}^{eff}$ although it decreases slightly with interstitial supersaturation. Since the experiments we consider have an interstitial supersaturation ($C_{\rm I}> C_{\rm I}^*$), the importance of vacancy recombination is reduced. We thus set $\sigma_{\rm V}$ to zero in our simulations and allow $\sigma_{\rm I}$ to determine the extent of effective recombination.

Figures 3.8 and 3.9 show the results of the simulation of Griffin *et al.*'s [34] lateral OED experiment for the 5μm stripe-width at 900°C, with the former showing the effect of changing the segregation coefficient ($m_{\rm I}$) and the latter showing the effect of a changing diffusion coefficient in the inert oxide ($D_{\rm I}^{\rm SiO_2}$). In both these plots, supersaturation ratio is defined as the normalized ratio of supersaturation under the oxidizing stripe to that under the inert stripe, normalized to the supersaturation under the widest oxidizing stripe showing maximum OED. Detailed explanations for the calculation of this parameter can be found in Section 2.4.1. Both figures

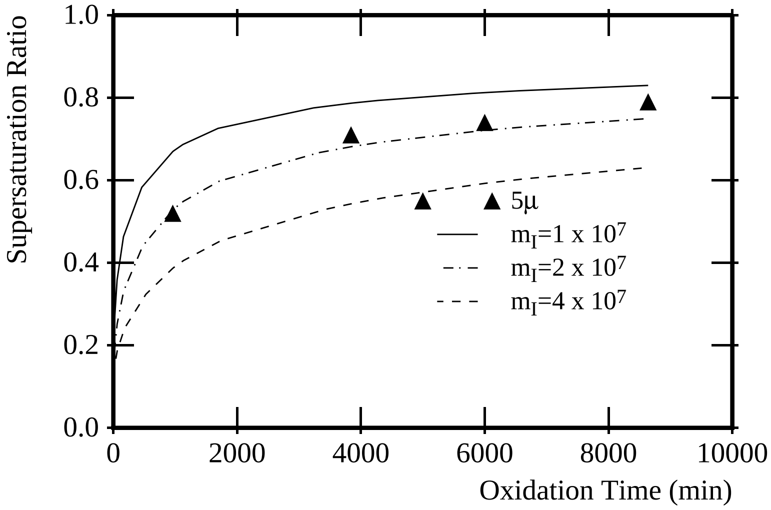

Figure 3.8: *The effect of varying* m_{I} *in the SUPREM IV diffusion solver for the example of Griffin et al.'s lateral OED experiment at 900°*C. *The stripe width chosen for the simulation is* 5μm.

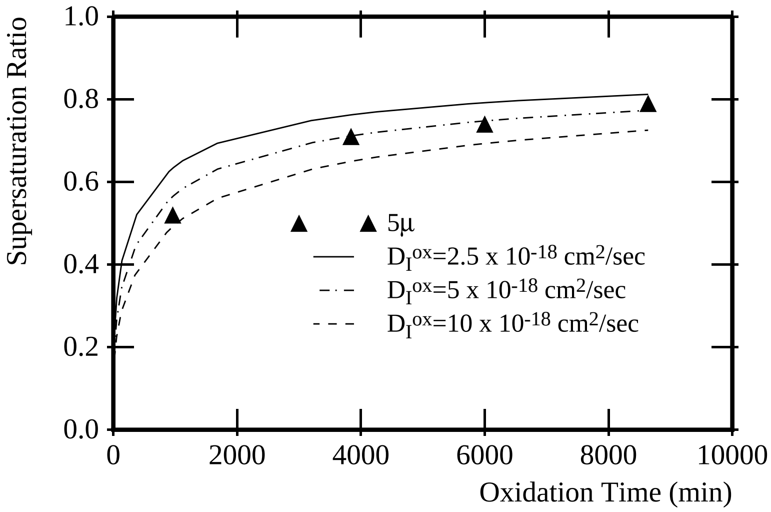

Figure 3.9: *The effect of varying* $D_{\mathrm{I}}^{\mathrm{SiO_2}}$ *in the SUPREM IV diffusion solver for the example of Griffin et al.'s lateral OED experiment at 900°*C. *The stripe width chosen for the simulation is* 5μm.

show similar trends of decreasing supersaturation ratio as the value of the variable parameter, either m_I or $D_{\mathrm{I}}^{\mathrm{SiO_2}}$, is increased, with the results more sensitive to m_I. This similarity can be explained physically since either an increased segregation coefficient of interstitials to the oxide or greater diffusion within the oxide provides an increased drive for interstitials to move into the oxide side of the Si/SiO_2 interface and must result in a decreased supersaturation on the silicon side of the interface. In our actual simulations (Chapter 8) we do not vary $D_{\mathrm{I}}^{\mathrm{SiO_2}}$ since we use a value extrapolated from Celler *et al.*'s experiments, as discussed in Section 3.2. An error in the extrapolated value of $D_{\mathrm{I}}^{\mathrm{SiO_2}}$ would therefore be compensated for by a change in the segregation coefficient.

In summary, in Section 3.3, we simulate the effect of varying the relevant parameters determined from Sections 3.1 and 3.2. The results of these initial simulations, therefore, allow us to select an appropriate parameter set that is then used in the actual simulation presented in Chapter 8.

Chapter 4

Buried Layer Study: Bulk Interactions in Epitaxial Silicon

A particularly attractive experiment for quantifying bulk point defect properties is to measure the dependence of oxidation-induced interstitial supersaturation on depth into the wafer (distance from the oxidizing wafer surface). Such an experiment markedly reduces the effects of interactions at nonoxidizing interfaces and can be performed by using buried dopant marker layers whose measurable diffusion enhancement can be directly related to interstitial supersaturation. A previous experiment using phosphorus and antimony buried layers [33], found no significant difference between diffusion at depths of 10 and 40μm and led to an estimated lower bound of $2.7 \times 10^{-8}\,\mathrm{cm}^2/\mathrm{s}$ for interstitial diffusivity. In this work, we use a shorter oxidation time (60 min versus 200 min) and a slightly larger range of buried layer depths, and are able to measure a decrease in enhanced phosphorus diffusion with depth. We analyze the results both in terms of a simple model (without recombination, as in most previous work) to calculate an *effective* interstitial diffusivity, as well as with a model including bulk recombination of interstitials and vacancies, which leads to a calculation of the ratio of the concentration of vacancies to that of interstitials in equilibrium.

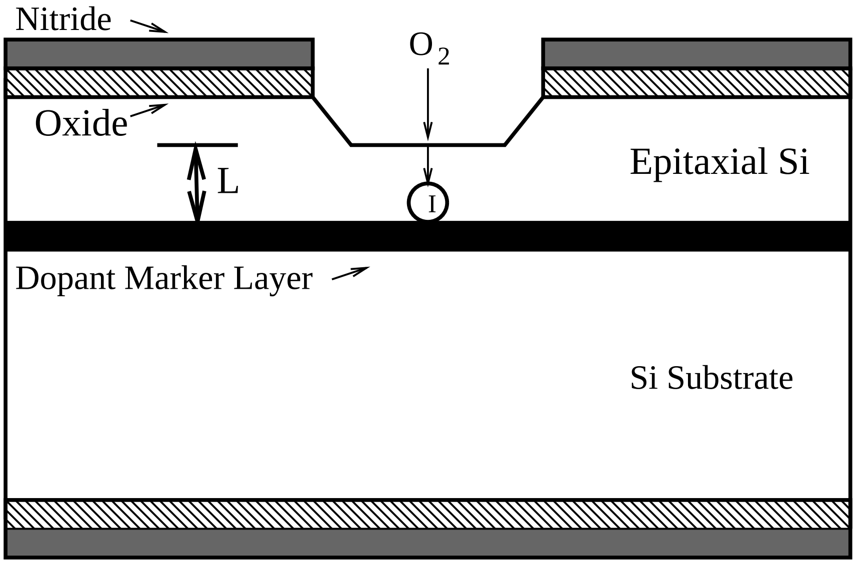

Figure 4.1: *Test structure prior to final oxidation.*

4.1 Experimental Procedures

For our experiments, the starting substrates were high resistivity (>500 Ω-cm) phosphorus-doped <100> float-zone silicon. The wafers were implanted with phosphorus at 150keV with a dose of 2×10^{13}cm^{-2} (small enough so that the material remained intrinsic at processing temperatures). After implant annealing, epitaxial silicon was grown on the implanted substrates at 1040°C for 80 minutes to yield 45μm of epi. Following epi-growth, a 1500 Å thermal oxide was grown and a final 1500 Å nitride film was then deposited using low pressure chemical vapor deposition. The oxide/nitride multilayer serves as an oxidation barrier. The wafers were patterned to yield 1 cm^2 openings in this SiO_2/Si_3N_4 multilayer, with each wafer cleaved such that every sample piece had one window. The exposed silicon in these windows was etched anisotropically in KOH to varying depths to obtain the final test structures, for which the distance of the buried layer from the exposed silicon surface (L) ranged from 6 to 45μm. A schematic of the resulting test structure is shown supersaturation in Figure 4.1. As a final step, the buried layer samples were diffused in dry O_2 at 1100°C for 1 hour.

Spreading resistance measurements (See Appendix A) were used to measure the doping profiles for each membrane, both before and after the final oxidation. The buried layer membrane thickness was determined by measuring the distance of the peak of the phosphorus doping profile from the oxidizing Si-SiO_2 interface. SERAPES, SUPREM IV and PROFILE were used as described in the Appendix A and for each membrane thickness, the values of phosphorus diffusivity which resulted in the best match to the measured profiles were calculated.

4.2 Results and Discussion

Our experimental results show a decrease in phosphorus diffusivity with increasing buried layer depth, in contrast with a previous measurement of buried layer diffusion by Griffin *et al.* [33], which found no dependence on epi thickness beyond the estimated error in their experiment of $\pm 5\%$. In this work, we found a difference of about 20% in the phosphorus diffusivity between depths of 6 and 45μm.

Since we use a shorter oxidation time and a slightly larger range of buried layer depths, we expect the difference in the enhancement factors to be significantly larger than in the previous work. It is also possible that the quality of epi could play a significant role in the dependence of interstitial supersaturation on buried layer depth, as a similar experiment [19] performed in our laboratory using visually poorer epitaxial films (rougher surface morphology when observed under the microscope) obtained from a different source gave a much stronger dependence of supersaturation on depth.

Figure 4.2 plots typical spreading resistance profiles for buried layers at 6 and 45μm, which shows the slightly reduced broadening we observed in the phosphorus profiles with increasing depth.

Dopant diffusivity can be written in terms of interstitial and vacancy components as in Equation(2.13), leading to the relationship of Equation(4.1).

$$\frac{\langle D_P \rangle}{D_P^*} \cong \frac{\langle C_{\mathrm{I}} \rangle}{C_{\mathrm{I}}^*}. \tag{4.1}$$

We compare our experimental results to two models, simple interstitial diffusion, with no recombination, and the coupled diffusion of interstitials and vacancies, in-

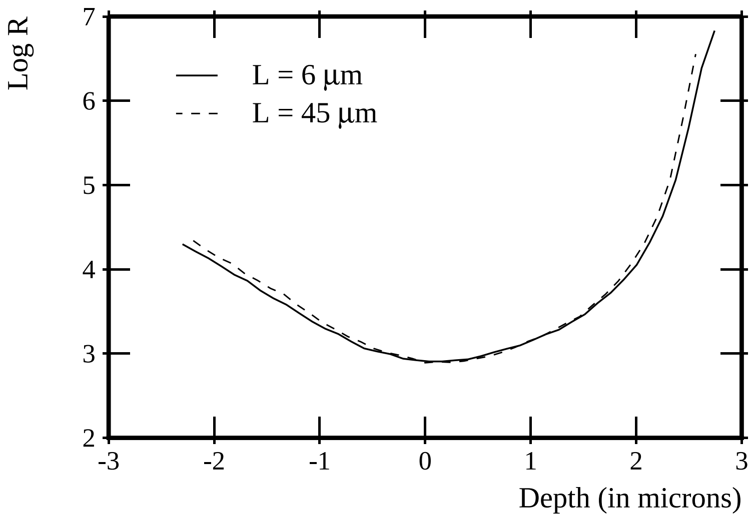

Figure 4.2: *Comparison of typical spreading resistance profiles at 6 and 45 μm. The resistance minima have been aligned for ease in comparison.*

cluding bulk generation/recombination processes. For example, recombination with vacancies can be expected to slow down the interstitial diffusion front, leading to a lower calculated effective interstitial diffusivity when Frenkel pair recombination is ignored in the calculation. For all simulations, the boundary condition at the oxidizing interface is modeled by interstitial generation and fast interface recombination, leading to interstitial supersaturation as a function of oxidation rate. The magnitude of the interstitial generation used in the simulations is determined from matching the enhanced diffusion data and is primarily dependent on the diffusion of the shallowest buried layer. At non-oxidizing SiO_2 film interfaces, we use a constant interface regrowth velocity for both interstitials and vacancies. However, for these experiments, interactions at non-oxidizing interfaces have a negligible effect on the results since the backside is a full wafer thickness ($\sim 500\mu$m) from the buried layers and the lateral non-oxidizing regions are several thousand microns away.

In order to compare our results to other work, our first model includes only simple interstitial diffusion (ignoring bulk recombination):

$$\frac{\partial C_{\rm I}}{\partial t} = D_{\rm I}\frac{\partial^2 C_{\rm I}}{\partial x^2}. \tag{4.2}$$

We use SUPREM IV to simulate the diffusion of interstitials during the oxidation process. The time-averaged interstitial supersaturation as a function of distance from the oxidizing interface is calculated from the simulations and compared to the experimental values of interstitial supersaturation calculated from buried layer diffusion. The PROFILE [66] optimizer is used to extract an effective interstitial diffusivity from the best fit. The resulting calculated effective interstitial diffusivity was $D_{\mathrm{I}}^{\mathrm{eff}} = 4.1 \times 10^{-8}$ cm^2/s, slightly larger than the lower bound of 2.7×10^{-8} cm^2/s at 1100°C reported by Griffin *et al.* [33].

The second model includes recombination of interstitials with vacancies, in addition to the diffusion of interstitials and vacancies. We solve the continuity equations for interstitials and vacancies in the bulk, (Equations 3.1 and 3.2) with the same boundary conditions as for the first model, again using SUPREM IV.

The solution to this coupled system of equations, together with the boundary conditions, yields the interstitial supersaturation, which we then compare to our data.

In the simulations using the bulk recombination model, we assume that the interstitial diffusivity is the fast value of $D_{\mathrm{I}} = 6.7 \times 10^{-7}$cm^2/s at 1100°C obtained from metal gettering experiments [6], and we use a rapid recombination rate ensuring $C_{\mathrm{I}}C_{\mathrm{V}} \cong C_{\mathrm{I}}^*C_{\mathrm{V}}^*$ as observed experimentally [36]. The values of C_{I}^* and D_{V} were chosen so that the $C_{\mathrm{V}}^*D_{\mathrm{V}}$ and $C_{\mathrm{I}}^*D_{\mathrm{I}}$ products are consistent with silicon self-diffusion data [83], although for the conditions simulated, the results were nearly independent of D_{V}.

The equilibrium ratio of vacancies to interstitials, $C_{\mathrm{V}}^*/C_{\mathrm{I}}^*$, determines the decrease in effective interstitial diffusivity due to recombination with vacancies. For small values of this parameter, recombination has little effect. As $C_{\mathrm{V}}^*/C_{\mathrm{I}}^*$ increases, more and more interstitials must go to annihilating the vacancies before the interstitial concentration can rise. The result is a stronger dependence of interstitial concentration on depth, which can be interpreted as a smaller effective interstitial diffusivity.

Figure 4.3 shows simulation results from solving Equations 3.1 and 3.2 for a series of times at 1100°C. The surface concentration drops as a function of time because the oxidation rate slows as the oxide grows. From such simulations, the time-averaged interstitial supersaturation as a function of the distance from the injecting interface

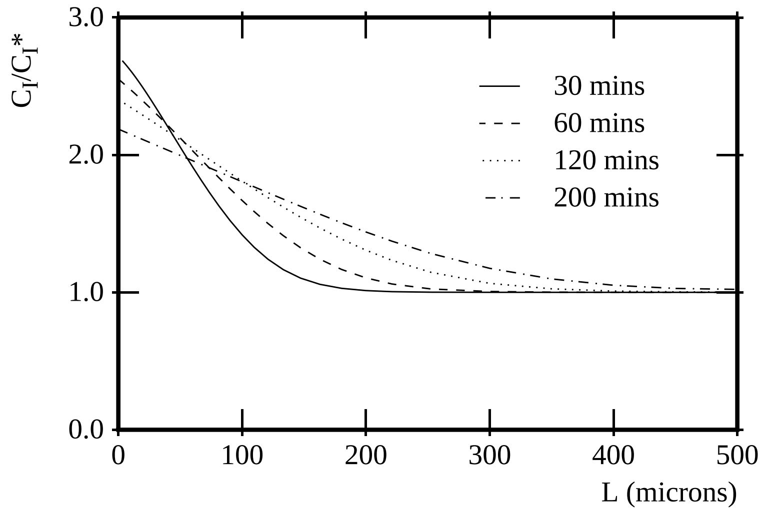

Figure 4.3: *Interstitial supersaturation as a function of distance into the wafer from the solution to Equations (3.1) and (3.2) for* $C_V^*/C_I^* = 84$ *after 30, 60, 120 and 200 minutes at 1100°*C.

can be determined and compared to the measurements of enhanced buried layer dopant diffusion. It is clear from these simulations that for shorter times a much larger variation of enhanced dopant diffusion with depth can be expected.

Figure 4.4 is a comparison of experiment and simulation for the diffusion of buried phosphorus marker layers during oxidation. The time-averaged interstitial supersaturation for a 60 min oxidation at 1100°C in a dry oxygen ambient is plotted as a function of the distance of the buried layer from the oxidizing interface. The supersaturation is defined as the ratio of the interstitial concentration at the buried layer depth to the concentration at equilibrium ($\langle C_I(L)\rangle / \langle C_I{}^*\rangle$). The error bars represent estimated error bounds on the calculated phosphorus diffusivity based on the accuracy of bevel angle measurements ($\pm 1\%$) and variations between multiple profiles on the same bevel. The best fit of the two models to the data give results which are indistinguishable, so only the model utilizing fast interstitial diffusion and including bulk recombination is included in Figure 4.4, as represented by the solid line. The fact that simulation results using the two models are equivalent demonstrates that rapid diffusion in conjunction with bulk recombination can indeed lead to experimental results which appear to be the result of a much smaller effective

Table 4.1: *Interstitial supersaturation as a function of buried layer depth.*

Buried Layer Depth (μm)	6	14	24	45
$\langle C_{\mathrm{I}} \rangle / C_{\mathrm{I}}^*$	2.15	1.85	2.01	1.74
$\langle C_{\mathrm{I}} \rangle / \langle C_{\mathrm{I}}(0) \rangle$	1.0	0.86	0.93	0.81

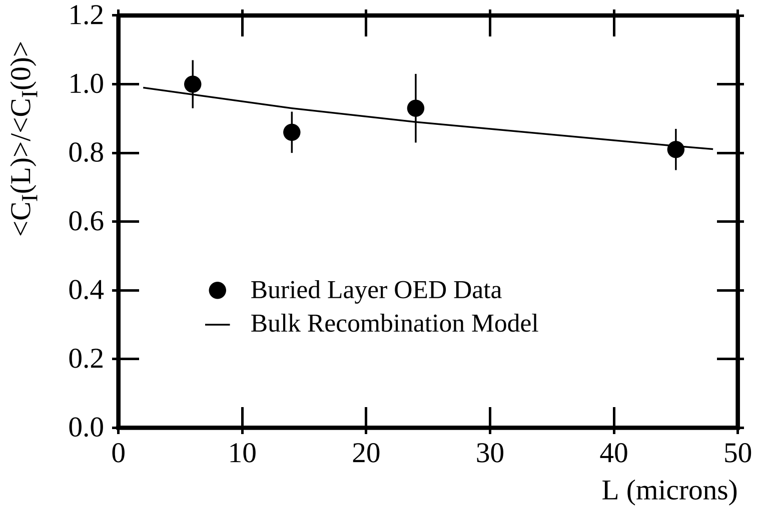

Figure 4.4: *Measured values of diffusivity enhancement for phosphorus buried layers during a 60 min oxidation at 1100°*C *in a dry oxygen ambient. This is compared to a simulation of time-averaged interstitial supersaturation as a function of distance of buried layer from the oxidizing interface. A model including bulk recombination with* $D_{\mathrm{I}} = 6.7 \times 10^{-7}$ *and* $C_{\mathrm{V}}^*/C_{\mathrm{I}}^* = 30$ *is used.*

diffusivity. Table 4.1 provides the data used in this graph.

We found that a value of $C_{\mathrm{V}}^*/C_{\mathrm{I}}^* = 30$ gave the best fit to the experimental data. This ratio is somewhat smaller than the value of 84 calculated by Tan *et al.* [83] at 1100°C based on silicon self-diffusion and metal diffusion, but appears reasonable given the approximations and experimental errors involved in both calculations. When the same parameters as obtained from our bulk-recombination model were used to simulate the experimental conditions of Griffin *et al.*, the predicted differences in average diffusivity calculated were significantly reduced, as expected for longer times (see Figure 4.3), and fell within the ±5% estimated error reported in that work.

4.3 Summary

In summary, we have measured the diffusion of phosphorus buried layers at depths of 6 to 45μm during oxidation of silicon at 1100°C. From the dependence of the diffusivity enhancement on the distance of the buried layer from the oxidizing interface, we have calculated an effective diffusion coefficient for silicon interstitials in epitaxial material of $4.1 \times 10^{-8}\text{cm}^2/\text{s}$, which is consistent with the lower bound calculated previously by Griffin [33].

These results, along with other reported calculations of effective interstitial diffusivity, can be explained consistently by considering the recombination of interstitials with vacancies. This reaction slows the movement of the interstitial diffusion front, since initially excess interstitials are annihilated by vacancies and only when the vacancy concentration is reduced can the silicon interstitial concentration rise. Thus, under conditions where bulk recombination is important, the value that would be calculated for effective interstitial diffusivity is greatly reduced. We have successfully modeled our results using an interstitial diffusivity derived from metal gettering experiments and considering Frenkel pair recombination. We find that we get good agreement with our measurements for $C_{\mathrm{V}}^*/C_{\mathrm{I}}^* = 30$ at 1100°C.

Chapter 5

Buried Layer Study: Bulk Interactions in Different Silicon Substrates

In this chapter, we study the effect of experimentally varying the distance of a buried dopant marker layer from the point-defect injecting surface (i.e., the oxidizing surface) and of using different types of silicon substrate material. Buried marker layers are used in our experiment to reduce the influence of surface interactions. To study the nature of these bulk interactions in different silicon substrates, we use Czochralski (CZ), intrinsically-gettered Czochralski and floatzone silicon substrates. The results show significant differences between the floatzone and the Czochralski substrates consistent with the bulk interactions of silicon interstitials with oxygen precipitates in CZ substrates.

5.1 Experimental Procedures

The starting substrates were lightly phosphorus-doped <100> floatzone (>500 Ω-cm) and Czochralski (10-20 Ω-cm) silicon. Excess oxygen in the CZ material precipitates out during thermal processing, thus generating excess interstitials [60]. To pre-

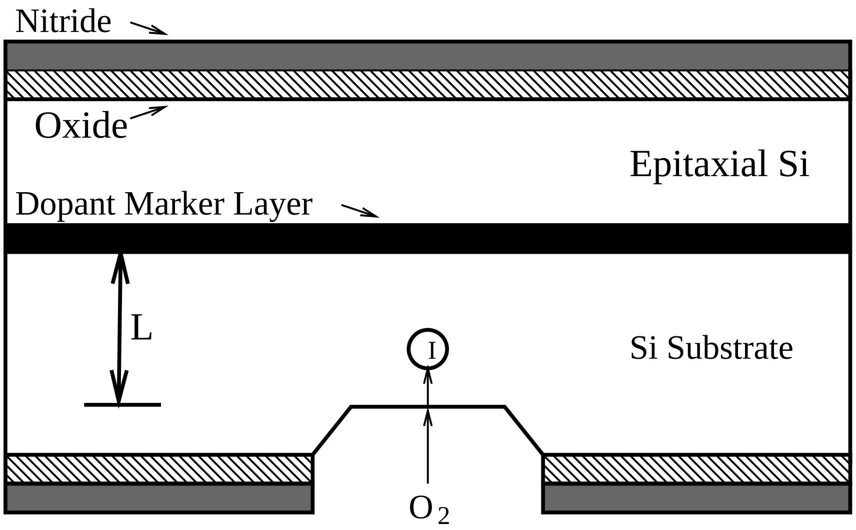

Figure 5.1: *Backside test structure prior to final oxidation.*

precipitate excess oxygen and avoid this problem, some CZ wafers were subjected to an initial low temperature nucleation process (4 hours at 750°C) followed by a high temperature growth anneal (1050°C), first in dry oxygen (4 hours) to grow a protective oxide and then in argon (50 hours). The treated and untreated CZ wafers as well as the as-purchased floatzone wafers were then implanted with phosphorus at 150KeV with a dose of $2 \times 10^{13}\text{cm}^{-2}$ (small enough to keep the material intrinsic at processing temperatures). After annealing, epitaxial silicon was grown on the implanted substrates at 1040°C for 80 minutes to yield 45μm of epi. Following epi-growth, a 1500Å thermal oxide followed by low-pressure chemical vapor deposited nitride multilayer was formed as an oxidation barrier. The wafers were patterned on the backside to yield 1 cm^2 openings in the oxide/nitride multilayer, with each wafer being cleaved such that every sample piece had one window. The exposed silicon in these windows was etched anisotropically in KOH to obtain the final membrane test structures with a range of distances of the buried layer from the exposed silicon surface (L). The resulting test structure is shown in Figure 5.1. A range of samples comprising different material types and membrane thicknesses were then oxidized in a dry oxygen ambient at 1100°C for either a short time (4 hours) or for a long time (20 hours) after saving one of each set to be used as a pre-oxidation starting sample. In each set, the spreading resistance technique was used to measure the resistance profile of the phosphorus implant in the pre-oxidation starting sample as well as in both the inert reference region and the oxidizing region of the oxidized sample. For each set of samples, the values of phosphorus diffusivity which resulted in the best match are calculated. Details of the spreading resistance procedure are provided in Appendix A.

5.2 Results and Discussion

From dopant diffusivity as given by Equation 2.13, Table 5.1 shows the interstitial supersaturation as a function of membrane thickness in the three substrates studied for the two oxidation times of 4 hours and 20 hours. The estimated error margin in each measurement is $\pm 7\%$ unless otherwise indicated. These are based on profile to profile variations on single and multiple bevels, as well as on the estimated accuracy in bevel angle measurements.

Simulated diffusion of the pre-oxidation profiles for each time (4 hour and 20 hour oxidation) were matched to the inert region profiles yielding an average value of 1.1 $\times\ 10^{-13}$ cm^2 sec^{-1} for D^*_{P}, the inert diffusivity of phosphorus. All other supersaturation calculations for each membrane thickness, as well as for the inert values in the Czochralski and gettered Czochralski samples, were performed by matching the floatzone inert doping profile with each sample's doping profile, calculated from the measured resistance profile using SERAPES [23].

Under nonoxidizing conditions, buried layer diffusion in the Czochralski substrates is larger than in the floatzone and intrinsically-gettered Czochralski material. This difference can be accounted for by interstitial injection due to oxygen precipitation as observed in previous work [48, 84] and summarized in Equation 2.10. Under oxidizing conditions, enhanced buried layer diffusion in the floatzone material decreases as the distance of the buried layer from the oxidizing interface increases, the trend becoming more apparent for the longer time oxidation. This can be explained by the larger membrane thickness increasing the bulk recombination volume, in addition to the somewhat larger relative influence of interactions at the nonoxidizing interface, which remains at a short fixed distance (epi thickness of 40μm).

Table 5.1: *Interstitial supersaturation as a function of membrane thickness in floatzone, Czochralski and gettered Czochralski substrates after 1100°C dry oxidation for 4 and 20 hours. All values are normalized to inert diffusivity in floatzone material.*

Substrate Material	4 hour oxidation		20 hour oxidation	
	Membrane thickness (μm)	Interstitial Supersaturation	Membrane thickness (μm)	Interstitial Supersaturation
Floatzone	100	1.23	100	1.49
	141	1.33	156	1.46
	265	1.20	284	1.17
	512	1.10	519	1.14
Czochralski	90	1.84	90	1.82
	131	1.80	131	1.70
	259	1.55	259	1.92
	Inert	1.67	Inert	1.88
Gettered Czochralski	104	1.50	145	1.14
	266	1.63	276	1.19
	510	1.13	514	1.25
	Inert	1.16	Inert	1.33

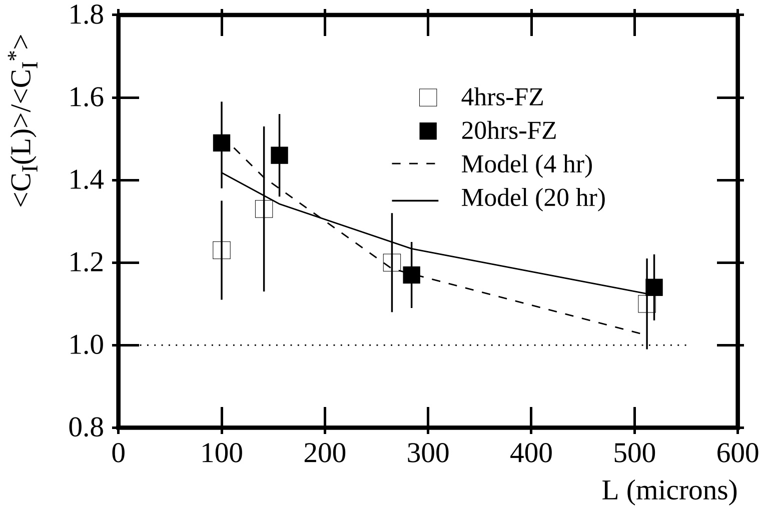

Figure 5.2: *Interstitial supersaturation as a function of membrane thickness in float-zone silicon substrates for 4 hour and 20 hour dry oxidation at 1100°C. The best fits to a model including bulk-recombination and surface regrowth are also included.*

Figure 5.2 shows the interstitial supersaturation as a function of membrane thickness in floatzone silicon substrates for 4 hour and 20 hour dry oxidation at 1100°C. Considering only bulk recombination (Equations 3.1 and 3.2) and surface regrowth/recombination (Equations 3.3 and 3.4), we show the best fits for each time. The parameters needed for this simulation fit are C_V^*= 4.3×10^{15} cm^{-3} and σ_I = 5.55×10^{-5} cm sec^{-1}, yielding C_V^*/C_I^* = 40 at 1100°C.

We then use the film-segregation model to obtain a numerical solution. We retain bulk recombination in the continuity equations (Equations 3.1 and 3.2) and surface regrowth processes (Equations 3.3 and 3.4) in the boundary conditions. In this model we use a segregation coefficient (Equation 3.9) to allow the inclusion of an additional boundary condition related to a preferential segregation of interstitials from the silicon into the oxide at the inert Si-SiO_2 interface. The diffusion coefficient for silicon in the oxide is given by Equation 3.16 and is included in the continuity equation for interstitials within the oxide (Equation 3.10). From a solution of this system of equations we calculate the segregation coefficient for interstitials between silicon and SiO_2 to be m_I = 1×10^6 using C_V^*/C_I^* = 30 as determined from the buried layer experiments in epitaxial silicon discussed in Chapter 4. Figure 5.3 shows the

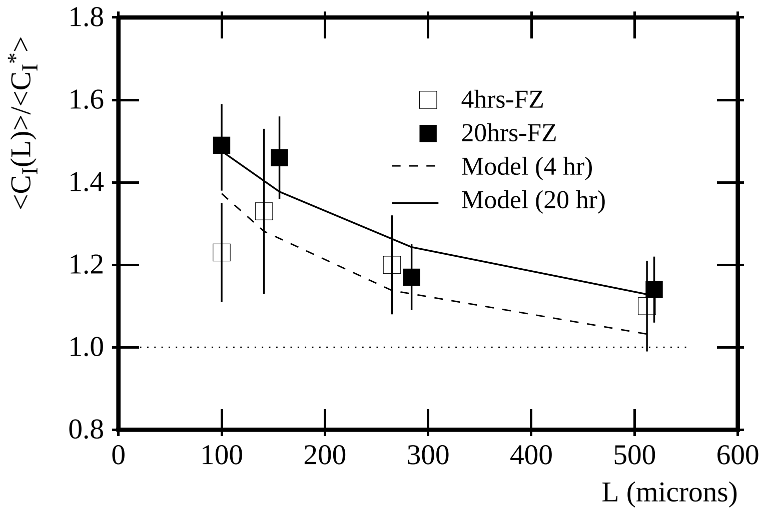

Figure 5.3: *Interstitial supersaturation as a function of membrane thickness in float-zone silicon substrates for 4 hour and 20 hour dry oxidation at 1100°C. The best fits to a model including film-segregation, bulk-recombination and surface regrowth are also shown.*

interstitial supersaturation as a function of membrane thickness in floatzone silicon substrates for 4 hour and 20 hour dry oxidation at 1100°C compared to the best fits in each case to the model including surface-film segregation, bulk-recombination and surface regrowth. A comparison of Figures 5.2 and 5.3 shows that the fit including the segregation model is better than the fit which includes only bulk recombination and surface regrowth, especially for the shorter time diffusion of 4 hours and for thinner membrane structures.

Figures 5.4 and 5.5 show the interstitial supersaturation as a function of membrane thickness in Czochralski substrates and intrinsically gettered Czochralski substrates, respectively, for the 4 hour and 20 hour dry oxidation at 1100°C. The untreated Czochralski wafers show both enhanced and retarded buried layer diffusion relative to inert conditions during oxidation, although in all cases the diffusivity is greater than in the floatzone samples.

In particular, enhanced diffusion is observed at the shorter time, while for the longer time the diffusion is retarded. These effects are consistent with the interactions of oxygen precipitation and surface oxidation. For the shorter time oxidation, very

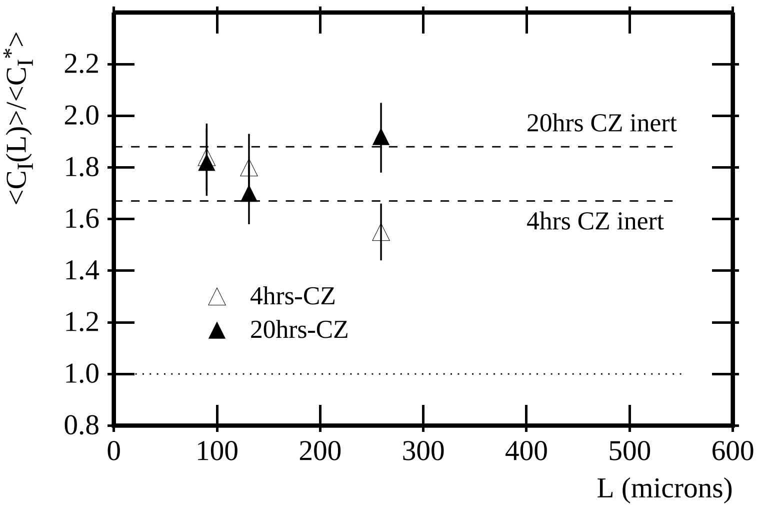

Figure 5.4: *Interstitial supersaturation as a function of membrane thickness in Czochralski silicon substrates for 4 hour and 20 hour dry oxidation at 1100°C.*

few oxide precipitates exist and newer ones are gradually being nucleated. Therefore, in addition to the interstitial injection due to oxidation, the forward precipitation process (Equation 2.10) injects interstitials and enhances phosphorus diffusivity. For the longer time oxidation, however, the interstitial oxygen has largely been converted to oxide precipitates. Additionally, the levels of interstitial injection from the oxidation mechanism has decreased. The existing precipitates, catalyzed by the lowered levels of interstitial injection, can form interstitial sinks during the backward oxide-dissolution reaction (Equation 2.10) in which silicon interstitials are consumed, resulting in the retarded phosphorus diffusion observed at the longer time.

The membrane thickness is an important variable. As it increases, the supersaturation decreases for the shorter time. At the end of the 4 hour oxidation the time-averaged value for the surface interstitial supersaturation ratio, $\langle C_{\mathrm{I}}(0)\rangle/C_{\mathrm{I}}^{*}$, is 2.09, which is higher than the value of 1.67 in the inert sample. Thus, the surface oxidation mechanism provides a higher interstitial supersaturation in comparison with the bulk oxygen precipitation mechanism, and as the distance of the buried layer from the injecting surface decreases, the supersaturation drops. For the 20 hour oxidation $\langle C_{\mathrm{I}}(0)\rangle/C_{\mathrm{I}}^{*} = 1.81$ which is nearly the same as the corresponding value of 1.88 in the inert sample and the experimental data falls near this range.

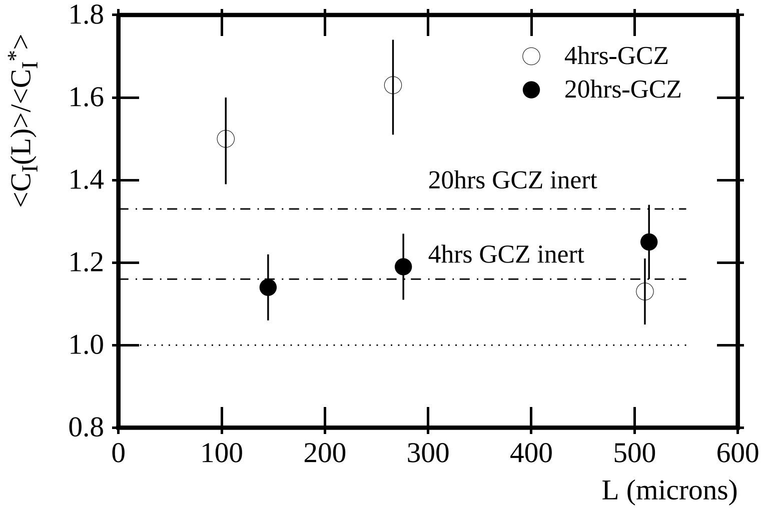

Figure 5.5: *Interstitial supersaturation as a function of membrane thickness in intrinsically-gettered Czochralski silicon substrates for 4 hour and 20 hour dry oxidation at 1100°*C.

The intrinsically-gettered substrates, in which most of the interstitial oxygen has presumably been precipitated prior to oxidation, showed mostly enhanced diffusion of the buried layer compared to inert diffusion for the shorter time. Here, at the end of the 4 hour oxidation the ratio $\langle C_{\mathrm{I}}(0)\rangle/C_{\mathrm{I}}^{*} = 2.09$ is much larger than the corresponding value of 1.16 in the inert sample. As with the Czochralski samples, the interstitial supersaturation is generally closer to the surface supersaturation for the thinner membranes. Additionally, this much lower value of supersaturation in the inert region is explained by the fact that there is no bulk source of interstitials since most of the oxygen precipitation is completed prior to the oxidation process. In contrast, the longer time oxidation showed retardation. At the end of the 20 hour oxidation, the ratio $\langle C_{\mathrm{I}}(0)\rangle/C_{\mathrm{I}}^{*} = 1.81$ is higher than the corresponding value of 1.33 in the inert sample. However, there seems to be little or no membrane thickness dependence and the interstitial concentrations are actually lower during oxidation. A possible explanation for this observation, as well as other irregularities in the results on Czochralski material may be the variations in bulk oxygen concentrations.

5.3 Summary

We have performed buried layer experiments in an attempt to reduce the influence of surface interactions of point defects. We have simultaneously investigated the effects of both, silicon substrate material and distance of injecting surface from the buried dopant marker layer, on dopant diffusion. Our experimental data from the floatzone samples, in conjunction with simulations using SUPREM IV, yielded a value of 40 for the ratio of equilibrium concentrations, C_V^*/C_I^* with net surface recombination velocity given by 5×10^{-5} cm/sec. When segregation of interstitials to surface oxide films was included and a ratio of C_V^*/C_I^* equal to 30 (obtained from our frontside epitaxial silicon buried layer data) was used in our SUPREM IV simulations, we found a value of $\approx 2\times10^5$ for segregation coefficient and a value of $\approx 2\times10^{-7}$ for net surface recombination velocity.

Finally, qualitative information has been extracted from the experimental data obtained from Czochralski and intrinsically-gettered Czochralski substrates, consistent with oxide precipitation mechanisms. Additionally, some information on the effect of distance from the injecting surface to the buried marker layer is obtained in each case.

Chapter 6

Surface Film Study: Oxides and Nitrides

Standard models used in parameter extraction have often either oversimplified or not included the interactions of interstitials with surface films. In this chapter, we examine the nature of the interactions of oxide and nitride films with silicon point defects. Diffusion measurements of dopant marker layers that are located at the surface of the silicon substrate, near the oxide or nitride films, can yield information about such interactions. Here, we report the experimental results obtained from surface dopant layer diffusion studies in both Czochralski and floatzone silicon.

6.1 Experimental Procedures

The starting substrates were 4-inch, <100>, n-type, being either 200-300 Ω-cm resistivity floatzone silicon or greater than 20 Ω-cm resistivity Czochralski silicon. A thermal oxide was grown at 1000°C using a a three step oxidation process with 5 minutes in dry O_2 followed by 5 minutes in H_2O and ending with 5 minutes in dry O_2, yielding 630Å of oxide. The wafers were implanted with phosphorus at 400keV with a dose of 2×10^{13}cm^{-2} (small enough so that the material remained intrinsic at processing temperatures). After implant annealing at 950°C for 30 minutes, stripes

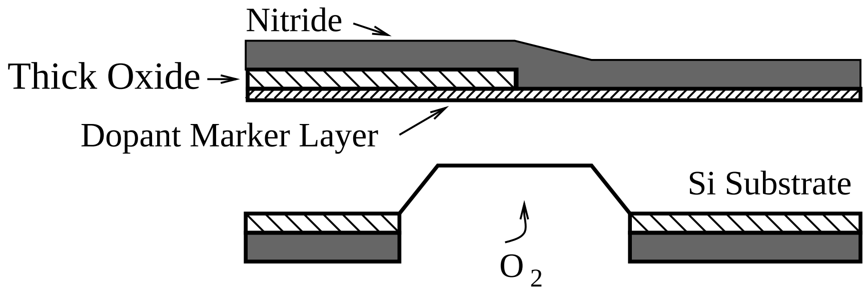

Figure 6.1: *Nitride/thick oxide/silicon versus nitride/silicon test structures prior to final oxidation.*

were patterned on the wafer frontside using photolithography. Each stripe was 3mm wide and the gap between stripes was 1mm wide. At this point in the processing, the floatzone and Czochralski wafers were divided into two groups each. The wafers in the first group were dipped in 7:1 BOE (Buffered Oxide Etch) until the entire 630Å thickness in the exposed 3mm wide striped region was etched away, while those in the second group were removed from the BOE etch-bath such that about 100-200Å of oxide thickness still remained in the 3 mm wide stripes. Oxide thicknesses were measured using an ellipsometer and was fairly uniform (±30Å) across the entire wafer. After stripping the resist, a 1500Å nitride film was deposited using low pressure chemical vapor deposition. The nitrided region serves the dual purpose of a silicon etch mask and an oxidation barrier. The backside of the wafers were patterned to yield 1-3 cm^2 openings in the Si_3N_4 layer, with each wafer cleaved such that every sample piece had one window. The exposed silicon in these windows was etched anisotropically in KOH to varying depths to obtain the final test structures, for which the distance of the surface dopant layer from the exposed silicon surface (L) ranged from 60 to 590μm. A schematic of the resulting test structures are shown in Figures 6.1 and 6.2. As a final step, these samples were diffused for 4 hours in dry O_2 at two different temperatures, 1000°C and 1100°C.

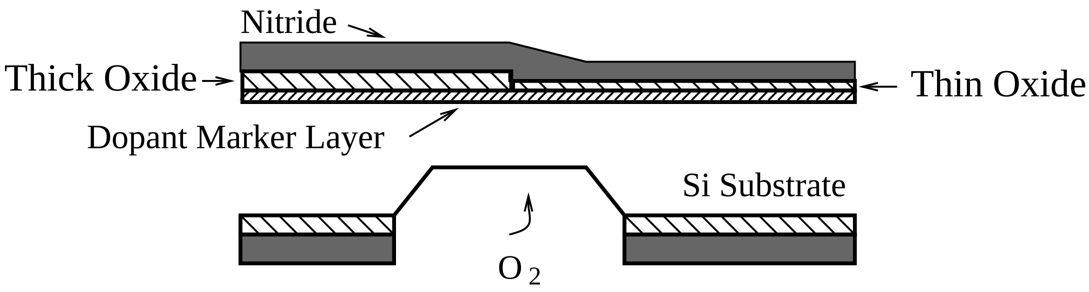

Figure 6.2: *Nitride/thick oxide/silicon versus nitride/thin oxide/silicon test structures prior to final oxidation.*

6.2 Results and Discussion

If the point-defect interactions at the surface oxide film are different from that at the surface nitride film, we expect to see a difference in the diffusion of the surface phosphorus marker layer beneath the $SiO_2/Si_3N_4/Si$ region compared to that beneath the Si_3N_4/Si region as observed in previous work [35, 57, 61, 86]. The structure displayed in Figure 6.1 attempts to investigate the presence of such differences. Furthermore, since we believe that segregation of interstitials to the oxide and the subsequent diffusion in that film occurs during interstitial injection, we investigate the effect of Si_3N_4/thick SiO_2/Si layer adjacent to the marker and compare with it the effect of Si_3N_4/thin SiO_2/Si adjacent to the marker layer. The structure displayed in Figure 6.2 attempts to compare the thick and thin oxide cases. In each pair of test structures, we perform backside oxidation and measure the diffusion of the dopant markers at the frontside surface beneath the two different kinds of film layers. Additionally, since membrane structures are used, the dependence of supersaturation on the distance between the marker layer and the injecting oxidizing interface is examined.

For the floatzone substrates, the comparison between the spreading resistance profiles beneath the Si_3N_4/thick SiO_2/Si multilayer for two different membrane thicknesses is shown in Figure 6.3. Also shown in the same figure are a similar comparison for the region beneath the Si_3N_4/Si multilayer and the comparison of profiles in each of the two regions for a 60μm membrane. Inert diffusion in both the domains are approximately the same and so an average inert diffusion coefficient of 1.0×10^{-13} cm^2/sec is calculated. For the thinnest membrane of 60μm, the diffusion enhancement beneath the Si_3N_4/SiO_2 region is calculated to be 1.53 and that beneath the bare Si_3N_4 region is 2.07.

Figure 6.4 shows the spreading resistance profiles in the thick and thin oxide regions respectively, for two different membrane thicknesses: 500μm and 101μm, after a 1100°C dry oxidation for 4 hours. The inert diffusivity is calculated to be $\approx 1\times10^{-13}$ cm^2/sec. Experimentally, since no significant differences are seen between the thick versus thin oxide after a 4 hour diffusion in dry O_2 at 1000°C, we attempted to perform the same diffusion experiment at a higher temperature of 1100°C, chosen to be high enough to allow diffusion of interstitials all the way to the nitride region in the thin oxide film but low enough not to allow the same to occur in the thick oxide film. Our rough calculations used $D_{\mathrm{I}}^{\mathrm{SiO_2}}$ extrapolated from Celler and Trimble's values at high temperatures, given by Equation 3.16. Therefore, for a 4 hour diffusion at 1000°C, a diffusion coefficient of interstitials in the oxide given by

$$D_{\mathrm{I}}^{\mathrm{SiO_2}} = 2\times10^{-17}\mathrm{cm}^2/\mathrm{sec}, \tag{6.1}$$

would yield an approximate distance traveled within the oxide as

$$\sqrt{Dt} = 50\,\text{Å}, \tag{6.2}$$

while at 1100°C for the same time, with

$$D_{\mathrm{I}}^{\mathrm{SiO_2}} = 4\times10^{-16}\mathrm{cm}^2/\mathrm{sec}, \tag{6.3}$$

the distance the interstitials would travel is calculated as

$$\sqrt{Dt} = 240\,\text{Å}. \tag{6.4}$$

Since the thin oxides are $\approx$ 100Å and the thick oxides are $\approx$ 630Å, a good choice of $\sqrt{Dt}$ would be one lying between 200Å and 600Å, justifying the 4 hour dry oxidation at 1100°C. In spite of the increased temperature, there was no measurable difference seen beneath the thick oxide versus the thin oxide as observed from Figure 6.4.

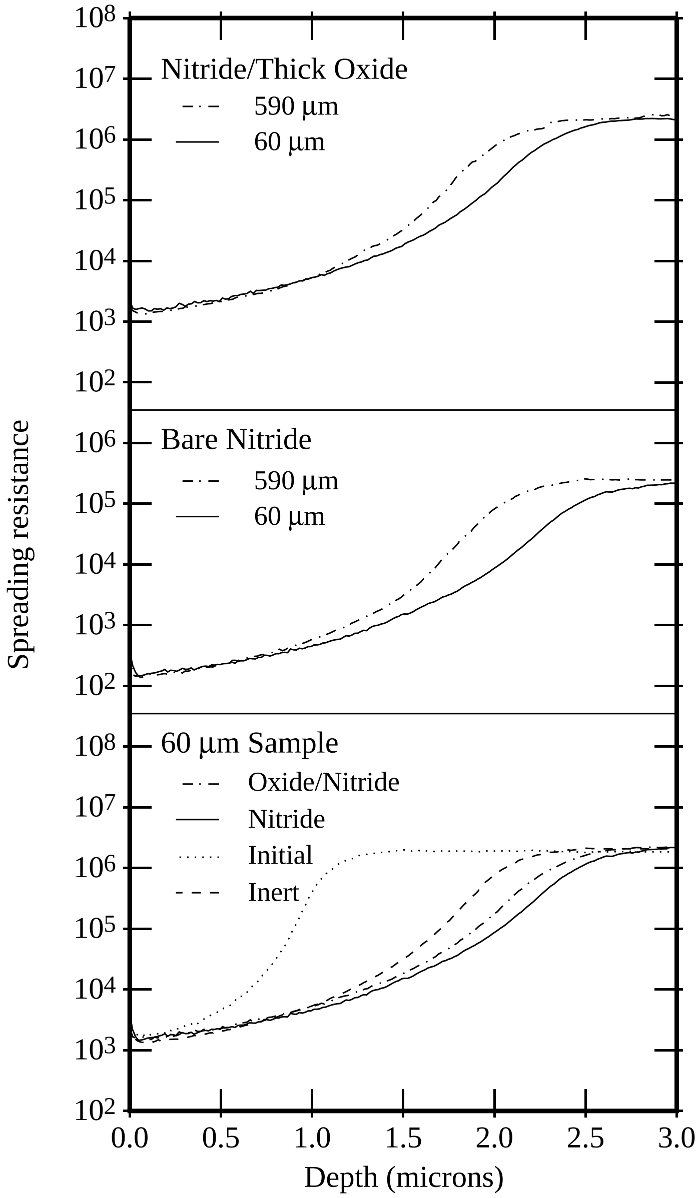

Figure 6.3: *Spreading resistance profiles in floatzone silicon samples, beneath a nitride/thick oxide multilayer and a bare nitride region, for two different membrane thicknesses: 590*μm *and 60*μm*, after a 4 hour dry oxidation at 1100*°C*. Also shown is a comparison of profiles in the two regions for the 60*μm *sample.*

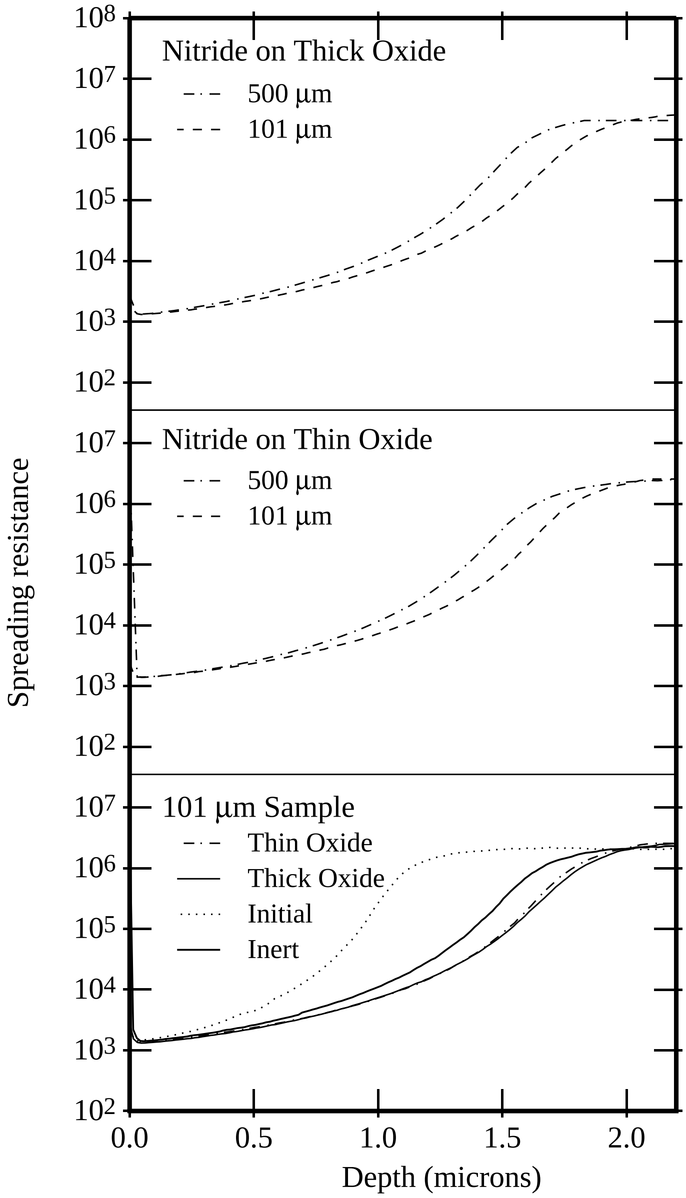

Figure 6.4: *Spreading resistance profiles in floatzone silicon samples, beneath nitride/thick oxide or nitride/thin oxide multilayers, for two different membrane thicknesses: 500*μm *and 101*μm*, after a 4 hour dry oxidation at 1000°*C*. Also shown are a comparison of profiles in the thick versus thin oxide regimes for a 101*μm *floatzone sample. The initial profile and the diffusion profile under inert conditions are included for reference.*

Figure 6.5 shows the calculated interstitial supersaturation near the inert oxide interface at the two experimental temperatures of 1000°C and 1100°C, for three different oxide thicknesses. The calculations are obtained as a result of a numerical solution to the interstitial continuity equation including both bulk recombination and the segregation of interstitials to the inert oxide film (Section 3.2). The interstitial supersaturation at the inert oxide interface depends on the *effective* recombination velocity for interstitials, $\sigma_{\mathrm{I}}^{\mathrm{eff}}$. This in turn depends on the segregation coefficient, m_{I}, the diffusivity of excess silicon in the oxide film, $D_{\mathrm{I}}^{\mathrm{SiO_2}}$, and on the interstitial interface regrowth velocity, σ_{I}. The relevant parameters used in the simulation are consistent with the values used throughout this work and are listed for easy reference in Table 6.1.

At 1000°C, there is no distinguishable difference in supersaturation between the 100Å and the 700Å oxide films, especially for short times. At longer times, there is some deviation between them but eventually the supersaturation saturates at long times not shown in this graph. The supersaturation at the 20Å film increases rapidly after about 2 hours, again saturating only at very long times not shown in this graph. This early interstitial build-up at the Si-SiO_2 interface near the 20Å oxide film can be explained by the close proximity of the reflecting SiO_2/Si_3N_4 interface to the Si-SiO_2 interface for the thinner 20Å oxide film but not for the thicker 100Å and 700Å oxide films. At 1100°C, the supersaturation for the 100Å oxide film starts to increase compared to the supersaturation for the 700Å oxide film, at about one or two hours, consistent with the calculation of Equation 6.4. However, as shown in Figure 6.5, the expected difference in interstitial supersaturation is less than 2% which is well below our experimental error estimates. The supersaturation in the case of the 20Å oxide film is much higher but it saturates in less than 4 hours, similar to the cases of the thicker oxide films.

The differences between the time-dependencies at 1000°C and 1100°C(Figure 6.5) are due to the fact that at short times the diffusion of interstitials into the oxide dominates in the effective interface recombination velocity term, while at longer times the interface regrowth velocity term dominates. The interstitial diffusivity, $D_{\mathrm{I}}^{\mathrm{SiO_2}}$, being smaller at 1000°C, explains the comparatively slower short-time separation of

Table 6.1: *A listing of simulation parameters at 1000°C and 1100°C.*

Temperature °C	C_I^* cm^{-3}	$D_I^{SiO_2}$ cm^2/s	m_I	σ_I cm/s	D_I^{Si} cm^2/s
1000°C	2.3×10^{13}	2.1×10^{-17}	6.4×10^{6}	1.8×10^{-5}	1.3×10^{-7}
1100°C	1.1×10^{14}	4.1×10^{-16}	2.6×10^{6}	2.5×10^{-3}	6.7×10^{-7}

the three curves and also the longer time taken to reach saturation.

Thus, the simulation results are consistent with the experimental observation of no measurable difference in the supersaturation level for the 100Å and 700Å oxide thicknesses, after a 4 hour diffusion, especially at 1000°C. However, for a 20Å oxide film the supersaturation level is higher and the differences between the 100Å and 20Å films can be expected to be distinguishable. A previous experiment of thermal nitridation of an oxide, performed by Fahey *et al.* [26], required in their SUPREM IV simulations that the effective recombination velocity beneath a nitrided oxide be more than an order of magnitude slower than beneath a nitride/350Å pad-oxide region (10^{-9} compared to 10^{-7}). The oxide thickness under the nitrided region is estimated to be only about 20Å and can be viewed as a limiting case of the thin oxide experiment performed here. We therefore believe that the thinner oxides ($\approx$ 20Å) present in Fahey *et al.*'s oxynitridation experiment (1000°C, 3 hour) were instrumental in their being able to see a difference in supersaturation levels for the thick versus thin oxide films. Additionally, since their experiments involve lateral OED, the distances over which interstitials must travel before they contribute to the measurements are only on the order of 10μm as against the 100-200μm distances involved in membrane structures. Thus, as discussed in Chapter 9, more experiments along the same lines with much thinner oxides and additional experiments using silicon isotopes may be required before the significance of segregation of interstitials to oxide films can be effectively tested.

Figure 6.6 shows a comparison of typical spreading resistance profiles beneath the Si_3N_4/thick SiO_2 multilayer in Czochralski silicon samples for three different membrane thicknesses: 220μm, 105μm and 70μm. A comparison of the resistance

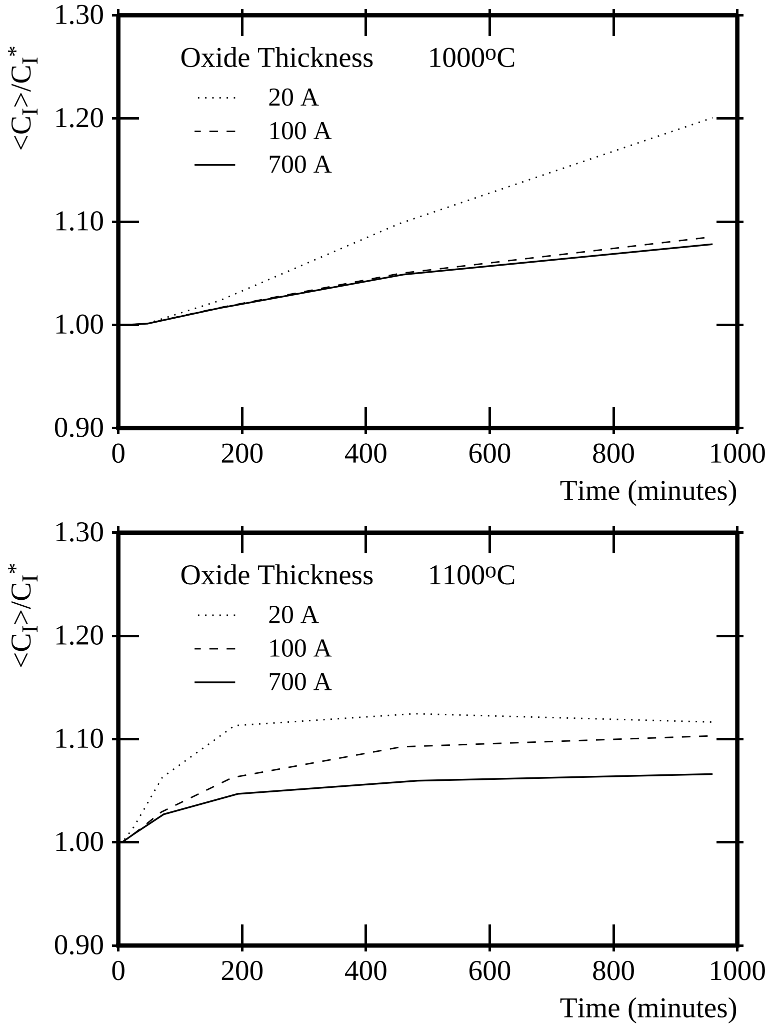

Figure 6.5: *Simulations of the interstitial supersaturation at the inert oxide interface at 1000°C and 1100°C as a function of time for three different oxide thicknesses.*

Table 6.2: *A comparison of phosphorus diffusivities calculated beneath nitride on thick oxide versus bare nitride.*

Sample Type	D in the Si_3N_4/Thick SiO_2/Si region (cm^2/s)	D in the Si_3N_4/Si region (cm^2/s)
Inert	1.1×10^{-13}	9.0×10^{-14}
590μm	1.0×10^{-13}	9.0×10^{-14}
60μm	1.4×10^{-13}	1.7×10^{-13}

profiles in the Si_3N_4/thin SiO_2 multilayer is also shown for the same membrane thicknesses and includes the inert diffusion profile. In the Czochralski samples, the spreading resistance profiles do not show any consistent trend as the membrane thickness is decreased. In addition, the diffusion beneath the oxidizing regions appear less than that beneath the inert region. This irregular behaviour may be attributed to the presence of a non-uniform distribution of bulk oxygen precipitate defects which act as sources and sinks for interstitials. Although a comparison of the profiles of the 70μm membrane structure (Figure 6.6) show that the diffusion beneath the thin oxide region is greater than that beneath the thick oxide region, no definite conclusions can be drawn since the repeatability of the process is not guaranteed in Czochralski substrates. This also provides further evidence that Czochralski substrates should be avoided in OED experiments.

6.3 Summary

We have measured the diffusion beneath three different types of surface films: Si_3N_4/thick SiO_2/Si, Si_3N_4/thin SiO_2/Si and Si_3N_4/Si, to investigate surface-film interactions in Czochralski and floatzone substrates. Membrane structures were formed to investigate the effects of distance of the injecting layer from the surface phosphorus marker layer. Finally, Table 6.2 compares the phosphorus diffusivities calculated beneath the Si_3N_4/Thick SiO_2 multilayer with that beneath the bare Si_3N_4 surface.

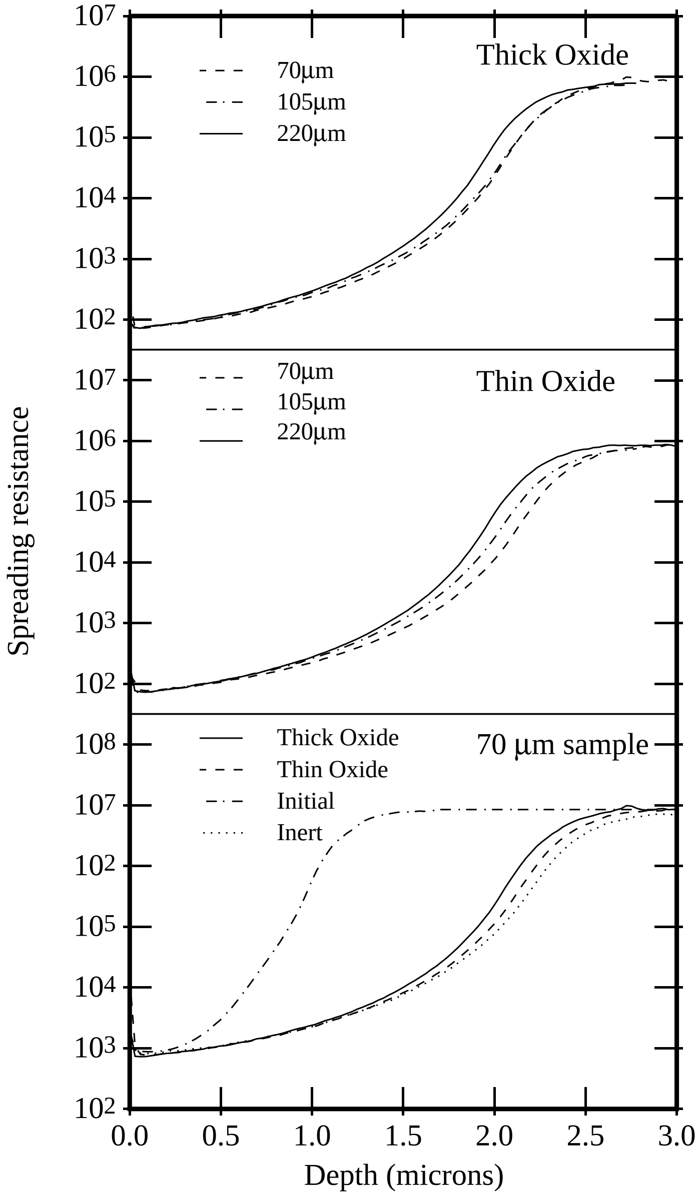

Figure 6.6: *A comparison of typical spreading resistance profiles in Czochralski silicon samples, beneath the nitride/thick oxide and the nitride/thin oxide multilayers for three different membrane thicknesses: 220*μm*, 105*μm *and 70*μm*. Also shown is a comparison of profiles in the two regions for the 70*μm *membrane sample.*

Chapter 7

Impact of Inert Ambient Annealing

During integrated circuit fabrication processing, Czochralski wafers are subjected to long time, high temperature heat treatments in inert gas ambients to facilitate intrinsic gettering of metallic impurities such as gold. Non-uniform defect formation has been observed during the annealing of silicon wafers with or without thin SiO_2 films over the temperature range of 750°C to 1175°C in vacuum [81, 55, 40, 39, 91, 74, 54, 53, 42], as well as in inert gas ambients, both pure [8, 68, 64, 38, 29, 70] and with low oxygen partial pressures [30, 73, 41]. The defects resulting from both vacuum and inert ambient annealing have been found to take the form of crystallographically defined etch-pits on wafer surfaces which deteriorate rapidly, thereby affecting point defect interactions at the Si-SiO_2 interfaces. The defect formation has been attributed primarily to oxide decomposition, in addition to active oxidation where low oxygen partial pressures are present, and has been found to be accelerated by the presence of pre-existing defects, in some cases caused by intentional damage [53, 38].

In this chapter, we examine the silicon wafer surface after a high temperature inert ambient anneal which was a part of an oxygen precipitation process in Czochralski silicon. Wafers with thin (< 500 Å) oxides are exposed to these ambients and the defect structures resulting from the high-temperature inert gas annealing of thin

SiO_2 films have been investigated. Specifically, Czochralski ⟨100⟩ silicon substrates with a 300 Å thermal oxide were subjected to a 60 hour anneal in argon at 1100°C. Following the anneal, the wafers were characterized via scanning electron microscope (SEM), ellipsometer, scanning Auger microprobe (SAM) and atomic force microscope (AFM). The defect structures included rounded octagonal voids as well as octagonal and rounded pyramidal etch-pits as reported previously. In addition, deep faceted pits covered by fractured or perforated surface films were observed. The defect morphology depended strongly on location, with the features near the wafer periphery being deeper and more strongly faceted. Based on these and previous experiments, we propose mechanisms for the development of the observed defects.

7.1 Experimental Procedures

The starting material was n-type ⟨100⟩ 10-20 Ω-cm phosphorus-doped, 4-inch Czochralski silicon prime wafers. A standard RCA clean was performed with 10 mins in H_2O:NH_4OH:H_2O_2 (5:1:1) at 80°C followed by a 15s dip in 50:1 H_2O/HF and a final ionic clean for 15 mins in H_2O:HCl:H_2O_2 (6:1:1) at 80°C. The wafers were then immediately transferred to the diffusion furnace and underwent a three stage process including a low temperature (750°C) argon anneal for 4 hours to facilitate nucleation of oxygen precipitates followed by a high temperature (1100°C) 5 min dry oxidation to grow a protective oxide and finally a high temperature (1100°C) argon anneal for 60 hours.

After measuring the apparent oxide thickness variation across the wafer using ellipsometry, the wafers were examined using a Hitachi S-800 as well as a JEOL-6100 scanning electron microscope (SEM) before and after removal of the surface oxide in a buffered oxide etch solution. A high voltage (25kV) was used to improve the resolution and a thin Au or Au-Pd alloy film sputtered on some samples formed a conductive coating which eliminated charge build-up on the otherwise insulating portions of the surface. Scanning Auger microprobe studies were also performed to characterize the chemical composition of the surface. Measurement of the defect depth were made using an Olympus optical microscope with a maximum magnifica-

Table 7.1: *Summary of radial variation of oxide thickness, defect density, size and shape.*

Region	A	B	C	D
Radius (mm)	0-99.2	99.2-100.5	100.5-101.3	101.3-101.6
Oxide Thickness (Å)	~240	≤100	~350	≥500
Defect Density (cm^{-2})	7 $\times 10^4$	1.5 $\times 10^4$	7 $\times 10^4$	5.5 $\times 10^4$
Dominant Defect Type	shallow octagons	octagonal defects	deep pyramidal pits	pits covered by perforated and fractured films

tion of 800X as well as with a TopoMetrix TMX 2000 atomic force microscope.

7.2 Results

Based on oxidation kinetics data [59], we expect a uniform oxide thickness of about 300 Å at the end of the second step in the process (5 min at 1100°C in dry oxygen). However, the oxide thickness measured by ellipsometry following the final 60 hour inert ambient anneal was quite non-uniform and manifested an approximately radial pattern. As is summarized in Table 7.1, the oxide near the center of the wafer measured about 240 Å. The apparent thickness dropped to less than 100 Å approaching the wafer periphery, and finally, increased again near the wafer edge. The extreme edges of the wafer showed the highest apparent oxide thickness (~ 500 Å). The ellipsometric measurements, particularly in areas of high defect density, should be treated with great caution acknowledging that the roughness of the film interfaces can cause substantial errors in the measurement [41, 20].

Scanning electron micrographs were made at several locations on the sample to characterize the defect structures and illuminate important aspects of the decomposition process. Table 7.1 summarizes these observations. Furthermore, the defect-density and dominant defect structure are tabulated in Table 7.1 as a function of

Figure 7.1: *Shallow octagonal defects prevalent near the center of the wafer (Region A), manifesting either a flat, uniformly textured surface (a) or a central depression (b).*

radial location, although it is important to note that the visually hazy regions near the wafer-edge, which are comprised of a large density of deeply etched defects, are concentrated in the lower two-thirds of the wafer, closer to points where the quartz wafer carrier contacted the silicon wafer.

Region A extending from the wafer center to a radius of about 99.2mm, has an average defect-density of 7×10^4 cm^{-2}, comprised mainly of shallow octagonal defects. As illustrated by the SEM micrographs in Figure 7.1, the defects in this region either display a uniformly textured surface or a central depression with an otherwise relatively smooth surface.

Region B, which is an annulus from a radius of 99.2mm to a radius of 100.5mm on the wafer, displays deeper octagons about 2-3μm deep and about 40μm wide, at an average defect-density of 1.5×10^4 cm^{-2}. Here, the defects appear as rounded

Figure 7.2: *Shallow octagonal defects of region B seen in plan-view at 200X (a) and at 950X (b).*

octagons, as seen in Figure 7.2(a). We can also see that these defects, like all the defects observed in this work, are oriented such that their sides are aligned in the $\langle 110 \rangle$ direction. A more detailed picture of these defects in Figure 7.2(b) reveals them to be shallow octagons having textured sides with a center that has a great deal of structure to it. Their depth as measured using an atomic force microscope is about 2-3μm.

The primary defect in Region C, which extends over an annulus from a radius of 100.5mm to a radius of 101.3mm, are deep rounded pyramidal pits with a density of about 7×10^4 cm^{-2}. The pits are about 6-8μm deep and 30μm wide and have highly textured sides as seen from Figure 7.3. These rounded pyramidal defects are similar to those previously observed by Reisman *et al.* [68, 70] and Hofmann *et al.* [40, 39].

Finally, Region D, which extends over a 0.3mm span at the wafer-edge, shows two unusual moderately deep defect morphologies at an average density of 5.5×10^4

Figure 7.3: *Rounded pyramidal etch-pits of region C.*

cm^{-2}. The most striking defect morphology seen here is illustrated in Figure 7.5(a), which shows the perforation of a surface film revealing a void beneath. As seen from Figure 7.4, the thin perforated film appears to be the initial thin SiO_2, since scanning Auger microprobe analysis identifies the film as oxide-like in nature, and the thickness of the film as estimated from the SEM micrographs is consistent with that of the initial oxide. As a further confirmation, after the sample is dipped in buffered oxide etch, the surface film is removed, revealing a faceted octagonal etch-pit about 7μm deep as seen in Figure 7.5(b). The other unusual defect morphology present in region D is illustrated in Figure 7.6. There appear to be voids beneath the shallow rounded depressions as seen in the figure which are then revealed by the fracturing of the surface layer. The underlying void is similar in shape to the deep rounded pyramids seen in region C. In contrast to the thin perforated film shown in Figure 7.5, these films are about 0.3μm thick, much too thick to be the SiO_2 grown prior to the anneal.

7.3 Discussion

Previous experiments involving high-temperature annealing of silicon under UHV conditions or in inert ambients concluded that the predominant reaction causing pitting at high temperatures (750°C to 1175°C) is the oxide decomposition reaction [40, 39, 45, 54, 68, 70, 69, 73],

$$SiO_2 + Si \rightarrow 2SiO. \tag{7.1}$$

Reisman *et al.* [68, 70, 69] conducted inert ambient annealing experiments using purified argon with residual oxygen and water removed via titanium gettering. They showed through calculations that silicon sublimation is not a viable possibility, and by carefully excluding other sources, surface creep from the fused silica wafer carrier was shown to be the source of SiO_2 required for the above reaction on bare silicon wafers.

In this work, the initial oxide film provides an additional source of oxide for the decomposition reaction. In addition, Gelain *et al.* [30] observed that for very low

Figure 7.4: *(a) SEM micrograph showing regions 1, 2 and 3 as being the regions outside the defect area, in the perforated film and inside the etch pit, respectively. (b) Auger spectrographs from region 2 which is the thin perforated film covering the etch-pit.*

Figure 7.5: *(a) Perforated surface film covering void in region D and (b) octagonal faceted pit revealed after buffered oxide etch.*

Figure 7.6: *Fracture of surface over buried void.*

oxidant pressures, the active oxidation reaction

$$2\mathrm{Si} + \mathrm{O_2} \rightarrow 2\mathrm{SiO}, \tag{7.2}$$

dominates over SiO_2 growth leading to silicon etching. In our experiments, although high purity argon gas (99.999%) was used, no special effort was made to remove any residual oxygen or water vapor from the gas source, allowing the possibility of active oxidation.

Experimental observations of the retarded diffusion of phosphorus and the enhanced diffusion of antimony during inert ambient annealing of thin oxides [3], have been explained by invoking the oxide decomposition mechanism. Dunham has shown in previous work [16, 18] that these effects can be accounted for quantitatively by considering two limiting processes occuring during oxide decomposition: first, the transport of excess silicon, in the form of interstitials, from the silicon bulk to the Si-SiO_2 interface and second, the transport of silicon (or equivalently SiO), through the surface oxide to the ambient.

For relatively thick oxides on silicon, the transport of Si through the oxide to the ambient becomes the rate-determining step. Thus, decomposition proceeds more rapidly where the oxide is locally thin or where oxide defects enhance transport of Si through the oxide. This in turn, further thins the oxide and accelerates the decomposition process locally, resulting in the development of oxide pinholes. On the other hand, for very thin oxides on silicon, the transport of silicon interstitials from the bulk to the interface becomes the rate-determining step. At this point, the presence of bulk defects becomes very important since they can act as interstitial sources, again locally accelerating the oxide decomposition, forming oxide pinholes when the bulk defect reaches the surface and remaining buried bulk voids when they do not make it all the way to the surface.

Evidence that point defect diffusion in the bulk is a limiting factor in the case of thin oxides is presented by Lifshits *et al.* [55] who have shown that the activation energy of the decomposition of thin oxides is 4.2eV, which is similar to the 4.1-4.5eV activation energy for the silicon self-diffusion process [37, 47], but is much more than the 0.8eV activation energy [80] required for the oxide decomposition reaction of

Equation 7.1.

The radial nature of observed defect distribution may be attributed both to the way in which Czochralski silicon is pulled from its melt leaving the region just inside the edge with the largest number of defects, as well as to the fluid flow patterns in the furnace, allowing SiO to escape faster from the wafer-edge region and also minimizing entry of oxidant to the wafer-center region, thereby locally driving the oxide decomposition and active oxidation reactions further in the forward direction nearer the wafer periphery. The additional observation of larger concentrations of deeply etched pits seen in regions of the wafer near the silica wafer carrier are attributed to creep from the quartz providing an extra source of SiO_2 for the decomposition reaction [69]. The oriented octagonal or pyramidal defect shapes observed can be attributed to anisotropic etching of the lattice planes and are consistent with the slower etching of (111) planes compared to (100) planes.

In the center of the wafer, the wide and shallow defects observed in Figure 7.1(a), as well as the deeper defects seen in Figure 7.1(b), have depths that are much greater than can be accounted for solely by the oxide decomposition reaction of the initial surface oxide. An explanation for the deepening of the pits requires long-range creep from the wafer carrier or active oxidation due to residual oxidant in the ambient.

Similarly, in regions B and C, after the initial surface thin oxide is consumed, further deepening of the defects (Figures 7.2(b) and 7.3) can be explained by the combination of oxide decomposition via surface creep from the wafer carrier and the active oxidation reactions.

Finally, the buried defects observed in region D (Figures 7.5 and 7.6) can be accounted for by noting that as bulk defects act as interstitial sources (or vacancy sinks), they can develop into voids within the silicon. Once formed, the voids continue to act as interstitial sources, growing in size. For buried voids which grow to reach the interface, pinholes in the oxide can allow entry of oxidant species from the ambient, leading to active oxidation and further growth of the void. An example of this mechanism can be seen in the perforated structures of Figure 7.5(a), which cover faceted octagonal pits that can be exposed by etching as shown in Figure 7.5(b). Continuation of the decomposition reaction may also assist in the formation of these buried defects, however, it is difficult to explain how silica creep from the wafer carrier can play an important role when the initial surface oxide remains unconsumed. An example of buried voids which continue to grow but never reach the interface can be seen in Figure 7.6. These defects are eventually exposed when the surface is fractured, as can be seen in this figure.

The decomposition of the thin surface SiO_2 film via Equation 7.1, leading to the experimentally observed etch-pits, is explained by the segregation and then the migration of Si, through the SiO_2. This mechanism further supports the idea of segregation of excess Si to SiO_2 followed by diffusion therein, as discussed in Section 3.2, and provides some early physical evidence of the validity of the segregation model.

7.4 Summary

In summary, we have characterized the defect structures resulting from high temperature annealing of thin oxides on Czochralski substrates using SEM, atomic force microscopy (AFM), ellipsometry and a scanning Auger microprobe (SAM). In addition to the usual etch-pit defects seen in the past, we observed some unusual defect structures such as the perforated defect of Figure 7.5 and the fractured defect of Figure 7.6. We have explained the mechanism of formation of all the observed defects by invoking both the oxide decomposition reaction and the active oxidation reaction. In addition, the buried voids are explained in conjunction with interactions with bulk defects near the wafer periphery resulting from the Czochralski growth process.

Chapter 8

Comparison of Models to Broad Range Of Experimental Data

8.1 Introduction

In this chapter we compare the models developed in Chapter 3 to a wide range of experimental observations. We thus assess the effectiveness of the bulk recombination and film-segregation phenomena in predicting the spatial extent of point defect interactions. Although this experimental data previously gave large differences in calculated parameters, we obtain a single set of quantitative model parameters which can account for the full range of data in a consistent manner.

The wide discrepancies in calculated values of silicon interstitial diffusivity, observed in Figure 2.2, can be accounted for if important physical mechanisms like bulk recombination or segregation to surface films, that have been previously neglected, are included in the models. Both of these effects would reduce the supersaturation observed at short times for backside oxidation and 2D OED experiments and cause the calculated effective diffusivity to be much reduced in such experiments. The relevance and subsequent mathematical formulation of the different interactions are described in Chapter 3.

In our first set of simulations, we solve the coupled system of continuity equations for interstitials and vacancies in which the time rate of change of each of the point defect concentrations are dependent on a diffusion term and a Frenkel pair recombination term (Equations 3.1 and 3.2). We use interface boundary conditions in which point defect fluxes are proportional to their respective excess concentrations and the proportionality factor in each case is referred to as the interface recombination/regrowth velocity (Equations 3.3 and 3.4). As explained in Section 3.3, the vacancy interface recombination velocity, σ_{V}, is set to zero and the combined effects of interstitial and vacancy recombination at the interface are considered in an effective interstitial recombination velocity term, $\sigma_{\mathrm{I}}^{eff}$, given by Equation 3.17. We use a fast interstitial diffusivity as obtained from metal gettering experiments [6] and keep the $C_{\mathrm{I}}^{*}D_{\mathrm{I}}$ product fixed to be consistent with silicon self-diffusion data [83]. Interstitial generation and recombination at the oxidizing Si-SiO_2 interface is determined either from oxidation kinetics along with the known dependence of interstitial supersaturation on oxidation rate, or from experimental data at the oxidizing interface, if available. The numerical solution of this system of equations is labelled as the *bulk recombination model* simulation.

For the second set of simulations, we modify the boundary condition for interstitials, at the Si-SiO_2 interface, to include the concept of segregation of interstitials into the non-oxidizing oxide film (Equation 3.11). This segregation generates a flux of interstitials into the nonoxidizing SiO_2, with a decreasing gradient over time leading in turn to a flux into the film that decreases in time. The net result is an effective recombination velocity which decreases with time. We maintain the same boundary condition for vacancies in which the flux is dependent only on the interface recombination (Equation 3.4). We obtain a numerical solution of the same continuity equations in the silicon (Equations 3.1 and 3.2), while including this new boundary condition for segregation of interstitials and also solving for the diffusion of excess silicon in the oxide (Equation 3.10). The numerical solution of this system of equations with the inclusion of the modified boundary condition is labelled as the *film segregation model* simulation.

Both numerical simulations, the bulk recombination model as well as the film segregation model, yield the calculated interstitial supersaturation. We compare each of these model predictions to various data, both our own and that obtained from other sources in literature.

8.2 Simulation Results

All simulations were conducted using a modified version of SUPREM IV. The simulations were compared to experimental results from four sources. The first set of data was obtained from the frontside oxidation of membranes with a buried phosphorus marker layer (Agarwal and Dunham [2]). The second set was from the backside oxidation of membrane structures with a buried phosphorus marker layer (Agarwal and Dunham [1]), while the third set of data came from the backside oxidation of membranes with a frontside phosphorus marker layer (Ahn *et al.* [4]). Finally, the last set of data was obtained from the lateral OED of a boron marker layer beneath nonoxidizing stripes (Griffin *et al.* [31]). In all simulations, a rapid interstitial diffusivity calculated from metal diffusion studies was used [6].

Two models, each with two free parameters, were used in this work. The bulk recombination model includes Frenkel pair reactions in the bulk, but assumes a simple interface regrowth velocity at nonoxidizing interfaces. The film segregation model includes both bulk recombination as well as interstitial segregation to nonoxidizing SiO_2 films. Table 8.1 summarizes the values and sources of parameters used in the two simulations. To keep only two free parameters in the film segregation model, we used a value of $C_V^* = 7.14\times10^{22}\exp(-2.0\mathrm{eV/kT})$, which fixed the C_V^*/C_I^* ratio to 30 at 1100°C [2] while maintaining an activation energy of 2.0eV for C_V^* [83].

The comparison of the models, including bulk-recombination alone, and including bulk-recombination and film-segregation, to the experimental data set are shown in Figures 8.1 through 8.7. The data in each graph is shown by symbols. Solid lines represent the best fit of the bulk recombination simulation to the data, while the dashed lines represent the best fit of the film segregation model simulation to the data. Figure 8.1 is a comparison of experiment and simulation for the frontside

Table 8.1: *Parameters used in the simulations.*

Parameter	Pre-exponent	Activation Energy (eV)	Experiment Source	Reference
$C_{\mathrm{V}}^{*}D_{\mathrm{V}}$	2×10^{22} cm/sec	4.0	Self-Diffusion	[83]
$C_{\mathrm{I}}^{*}D_{\mathrm{I}}$	3×10^{25} cm/sec	4.8	Self-Diffusion	[83]
D_{I}	600 cm^2/sec	2.44	Gold Gettering	[6]
k_{IV}^{rec}	3.16×10^{-6} cm^4/sec	2.44	OED	[36, 67]
C_{V}^{*}	6.33×10^{22} /cm^3	2.0	Buried Layer OED	[2]
$D_{\mathrm{I}}^{\mathrm{SiO_2}}$	13.0 cm^2/sec	4.5	Thermo-migration	[7]

oxidation of a buried phosphorus marker layer in membranes that are 6, 14, 24 and 45μm thick. The value plotted is the time-averaged interstitial supersaturation (the ratio between the interstitial supersaturation at the indicated depth and the value at equilibrium) versus membrane thickness after a 60 min oxidation at 1100°C in a dry oxygen ambient.

Figures 8.2 and 8.3 show the fits of the bulk recombination and the film segregation models to the data obtained from our buried layer membrane OED experiments. The figures shown are for floatzone silicon substrates at the end of a 4 hour and 20 hour oxidation at 1100°C, respectively.

Figures 8.4 (a) and (b) are plots of interstitial supersaturation values from Ahn *et al.*'s backside oxidation experiments in floatzone silicon using 20, 55, 104 and 530μm membranes at 1100°C in dry oxygen ambient versus oxidation times ranging from 60 min (1h) to 3360 min (56h).

Finally, Figure 8.5 shows the normalized excess interstitial supersaturation ratio versus oxidation time at 900, 1000 and 1100°C, for two inert stripes in each case, normalized to the time-averaged enhancement in the wide oxidizing stripe regions where maximum OED occurs. The data points are derived from reported values of the lateral decay length calculated based on a range of stripe widths reported by Griffin [31]. Here, as in all the other simulations, the supersaturation at the oxidizing side is determined from published oxidation kinetics data [52] and OED/ORD models [46].

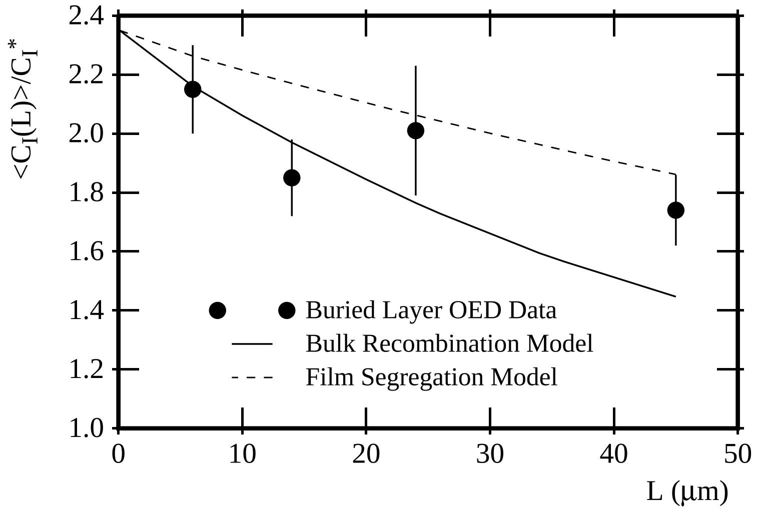

Figure 8.1: *Diffusivity enhancement versus depth for phosphorus buried layers during a 60 min oxidation at 1100°C in a dry oxygen ambient. Data from Agarwal and Dunham.*

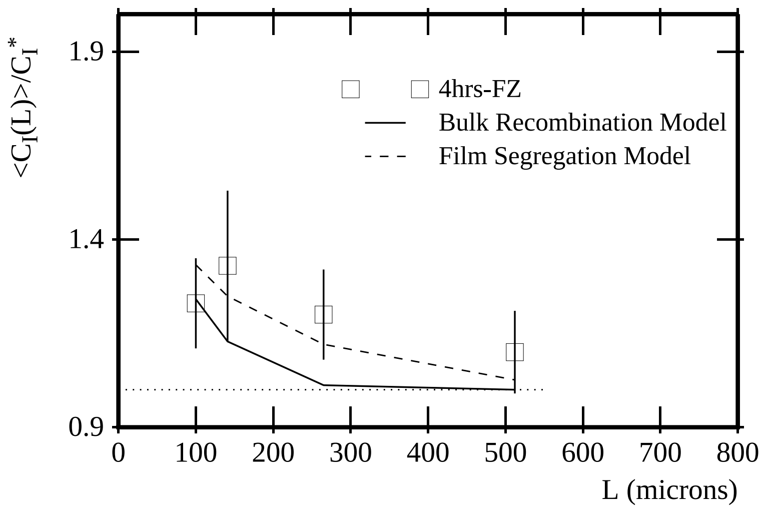

Figure 8.2: *Diffusivity enhancement versus depth for phosphorus buried layers at the end of a 4 hour oxidation at 1100°C in a dry oxygen ambient. Data from Agarwal and Dunham. Also shown are the fits to both models.*

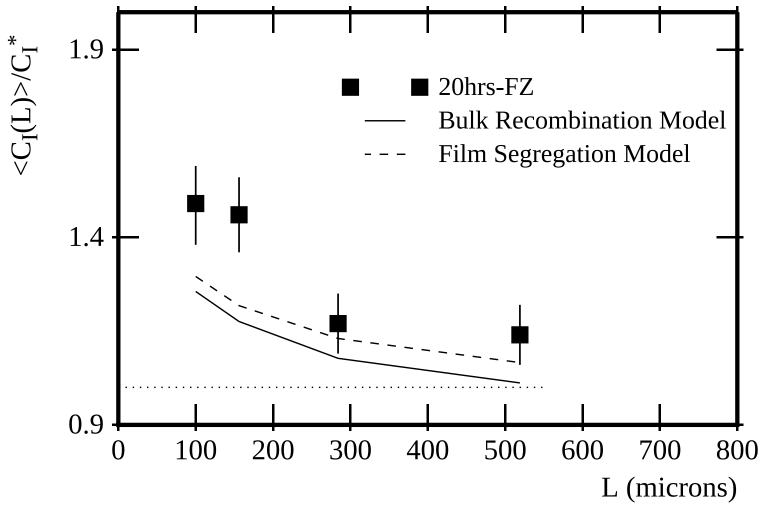

Figure 8.3: *Diffusivity enhancement versus depth for phosphorus buried layers at the end of a 20 hour oxidation at 1100°C in a dry oxygen ambient. Data from Agarwal and Dunham. Also shown are the fits to both models.*

Table 8.2: *Parameters calculated in the simulations when only bulk-recombination is included.*

Parameter Calculated	Pre-exponent	Activation Energy (eV)
σ_I	6.9×10^{18} cm/sec	6.04
C_V^*	4.4×10^{12} /cm^3	-0.98

Since the data is at 900, 1000 and 1100°C, we extract activated fitting parameters for each of the models. From the bulk recombination model fit, we determine values as listed in Table 8.2. From this model fit, a negative activation energy calculated for C_V^* is clearly unphysical from our fundamental understanding that the creation of vacancies (and interstitials) requires energy, thereby leading to a positive activation energy barrier. Further evidence of this fact is provided by a value of 2.0eV calculated by Tan and Gosele [83] as the activation energy barrier for vacancy creation. A particularly noticeable feature is that the calculated pre-exponential and the activation energy barrier for the silicon interstitial recombination velocity term are very large. The extracted parameters for the film segregation model are listed in Table 8.3. Here, the negative activation energy for the segregation coefficient is ex-

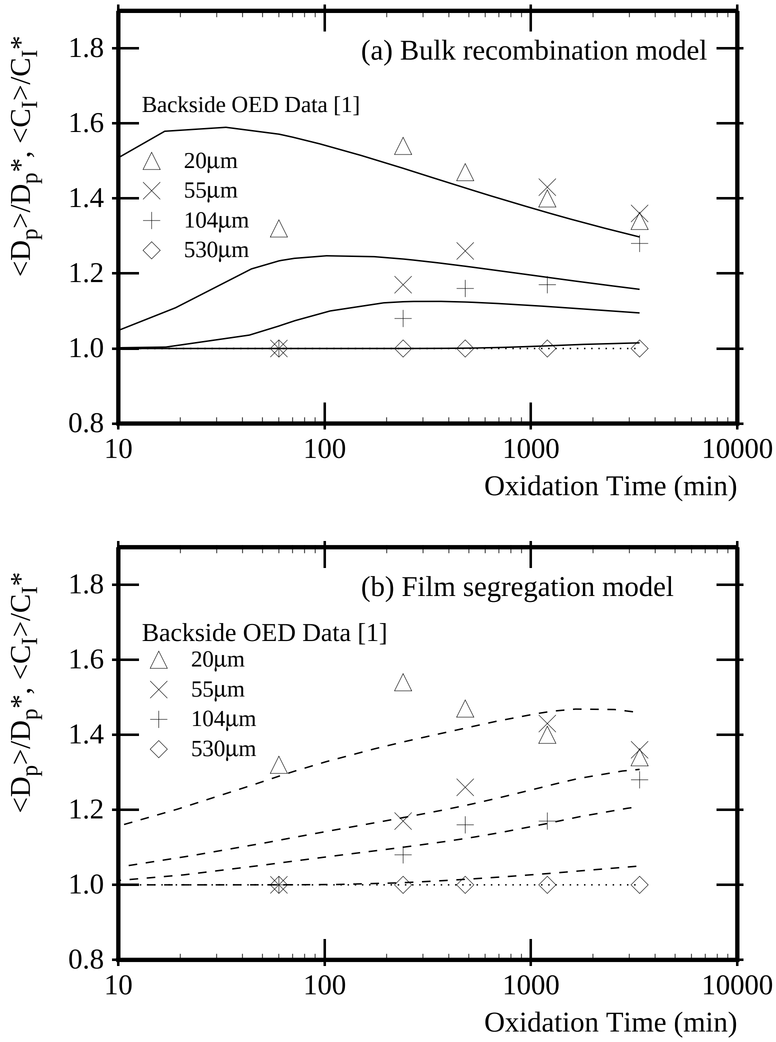

Figure 8.4: *Time-averaged phosphorus diffusion enhancement versus time during backside oxidation for a range of membrane thicknesses. Data from Ahn et al. utilizing 20*μm*, 55*μm*, 104*μm *and 530*μm *membranes at 1100*°C *in dry oxygen ambient as a function of oxidation time ranging from 60 min (1h) to 3360 min (56 h). The solid line in (a) and the dashes in (b) show the interstitial supersaturation values obtained from a SUPREM IV simulation using the bulk recombination model and the film segregation model, respectively.*

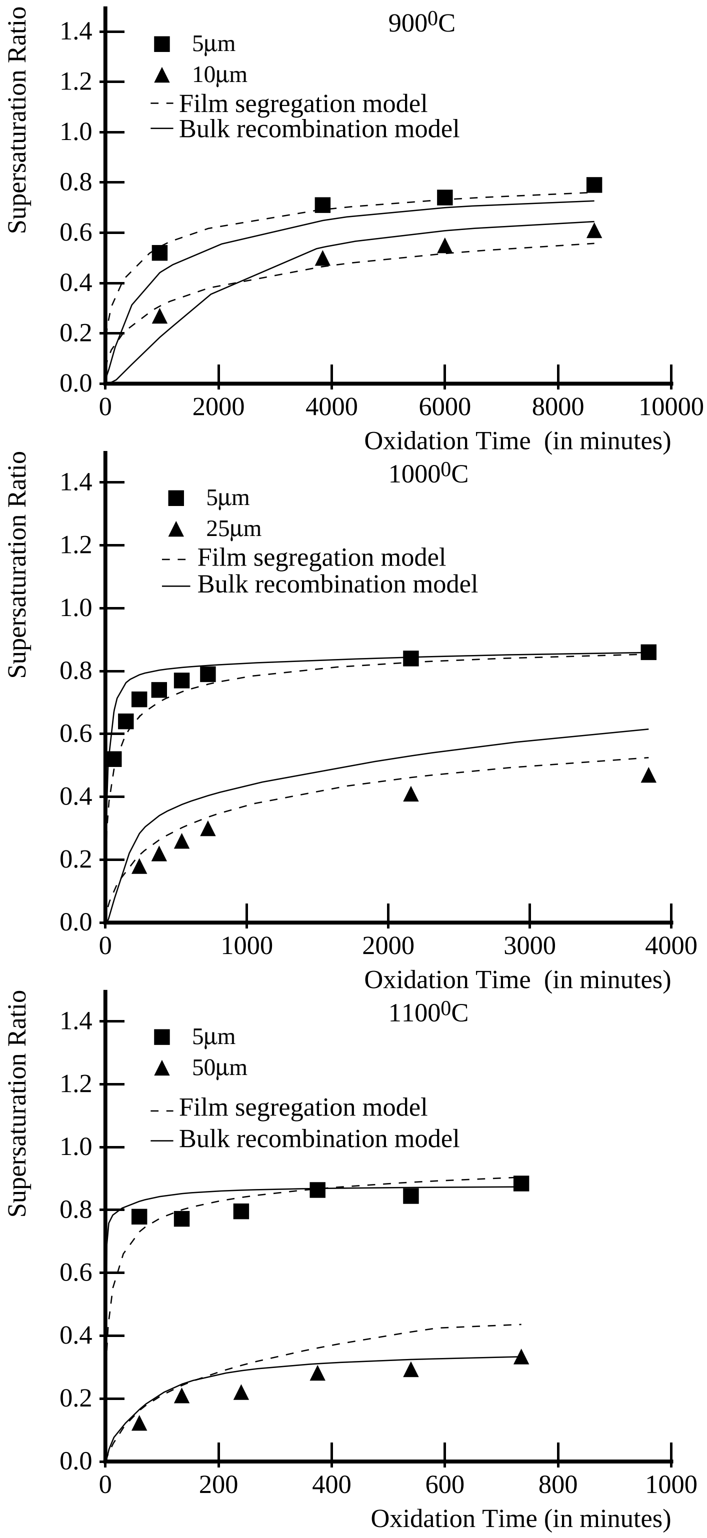

Figure 8.5: *Time-averaged boron diffusivity in the center of nonoxidizing stripes of given widths at 900, 1000 and 1100°C, plotted versus oxidation time. Data from Griffin. Normalized to the time-averaged enhancement/excess in the wide oxidizing stripe regions where maximum OED occurs.*

Table 8.3: *Parameters calculated in the simulations when bulk-recombination and segregation of interstitials to surface films are included.*

Parameter Calculated	Pre-exponent	Activation Energy (eV)
σ_I	2.5×10^9 cm/sec	3.65
m_I	69.2	-1.27

pected from the definition of m_{I} (Equation 3.9) since C_{I}^* has an activation energy of 2.36eV while $C_{\mathrm{I}}^{\mathrm{SiO_2}}$ is extrapolated to be only weakly temperature dependent [7]. The silicon interstitial recombination velocity, σ_{I}, has a smaller calculated pre-exponential as well as activation energy barrier when obtained from the film segregation model fit as compared to that calculated from the bulk recombination model fit. Thus the reasonable range of values for these two calculated parameters are further indication of the importance of including surface segregation of interstitials, in our physical model, in addition to bulk recombination.

As the figures show, the film segregation model accounts for the full set of data significantly better than the bulk recombination model. It is possible for the bulk recombination model to fit each of these data sets considered alone. However, to account for the slow rise in supersaturation, as a function of time, observed in Ahn's backside OED (Figure 8.4) and Griffin's 2D lateral OED (Figure 8.5) experiments, it is necessary to use a value of C_{V}^* which is orders of magnitude larger than the one utilized in matching the full set of data. In contrast, to account for the buried layer experiments (Figure 8.1), which show little or no change in interstitial supersaturation with depth, requires that C_{V}^* not be too large so that bulk recombination does not slow the diffusion front excessively. The film segregation model is able to better account for these differences because low effective diffusivity values are generally observed only when measuring interstitial supersaturations near nonreacting film interfaces, (see Table 2.2). However, bulk measurements of interstitial supersaturation, such as in the buried layer experiments and metal diffusion experiments respond much more rapidly in time. Considering film segregation, the interstitial concentration near the film interface cannot increase until the concentration in the film increases also. For strong preferential segregation to the film, as calculated in this work and also observed previously for oxides [18, 7], the rise in interstitial concentration is substantially delayed, accounting for the slow calculated effective interstitial diffusivities.

8.3 Summary

We find that it is possible to match a broad range of experimental data over a range of temperatures, from which widely disparate interstitial diffusivity values have previously been calculated, to models which include fundamental point defect interactions in the bulk and with surface films. In contrast to previous work, a single consistent set of point defect parameters are extracted. The model is consistent with the full range of experiments utilized to quantify interstitial diffusivity, including metal diffusion and gettering, the depth dependence of enhanced diffusion of buried layers, the lateral spread of oxidation enhanced diffusion, and enhanced diffusion during backside oxidation of membrane structures. The model provides a fundamental basis for predicting the spatial extent of point defect interactions in VLSI structures.

Chapter 9

Conclusions and Recommendations for Future Work

In this work we have performed a series of key experiments to measure the spatial extent of point defect interactions in silicon. Previously, there has been substantial disagreement on the values calculated for some important point defect parameters like interstitial diffusivity, interstitial recombination velocity at the inert oxide interface or equilibrium point defect concentrations. To account for the wide range of experiments which give rise to these discrepancies, we have proposed a model based on physical mechanisms that include relevant bulk and surface-film interactions. The main interactions we included were:

- Frenkel pair recombination
- Segregation of interstitials to surface films
- Surface regrowth.

The experiments we performed first focussed on investigating the bulk interactions of point defects using buried marker layers. We investigated four different types of silicon: epitaxial, Czochralski, intrinsically-gettered Czochralski and floatzone material. The results of our study using epitaxial silicon gave us a lower bound on interstitial diffusivity as well as an upper bound on C_{V}^{*}. From our comparison of buried layer results in Czochralski silicon and floatzone silicon material, we found that a large difference in the inert diffusion for the two materials may be explained by the oxygen precipitation mechanism in the Czochralski silicon bulk, which injects interstitials for times as long as 20 hours. The results from the floatzone silicon were used in conjunction with several other experimental data from literature, for the quantitative determination of a consistent set of parameters.

The next set of experiments investigated the effects of different surface film interactions. As a part of this study, we compared the effects of thick SiO_2 versus thin SiO_2 or thick SiO_2 versus bare nitride surfaces on interstitial supersaturations at each type of interface. From our results we were able to suggest a useful course for future experiments to provide further insights into the factors that can affect recombination kinetics at the interfaces.

Additionally, we studied long time and high temperature inert ambient anneals of thin oxides which lead to a deterioration of the silicon wafer surface. We were able to examine the nature of the defect structures on the surface microscopically and connect the presence of certain structures to the behaviour of point defects in the silicon.

Finally, a model including the important point defect interactions discussed above was proposed. We tested this model using a broad range of data taken both from the literature and from our own work. The data set chosen previously gave disparate results and no agreement could be reached about point defect parameters calculated based on each individual experiment taken separately. However, using a single consistent set of parameters, we were able to match this entire experimental data set to our proposed physical model.

9.0.1 Recommendations for future work

- Other experiments to further test the models that have been proposed in Chapter 3. These can include very short time OED measurements beneath very thin oxide films at temperatures lower than 1000°C. Submicron 2D profiling techniques [50, 15], that have recently begun to show a great deal of promise, may be necessary for observing the spatial extent of surface point defect interactions.

- Reverse short channel effects that have been observed experimentally can intuitively be explained by a physical model that includes segregation of interstitials to the gate oxides. A first step to a better understanding of this phenomenon would be to attempt to explain the phenomenon quantitatively using existing data. Also, further experiments that can test these ideas will contribute to the general understanding of this anomalous behaviour. Such experiments include:
  - Studies of surface-state measurements at a Si-SiO_2 interface to further examine the nature of segregation of interstitials into the inert oxide.
  - Measurements of OED directly beneath varying thicknesses of gate oxides (< 50 Å) for different levels of supersaturation in the channel. The different supersaturation levels can be accomplished by the threshold control implant and the source/drain implants.
  - Measurements of the threshold voltage under identical process conditions as discussed above to enable a direct comparison.
- Recent observations of non-Gaussian diffusion profiles during OED in SOI structures can also be attributed to segregation of interstitials to oxide films. By the exclusion of this mechanism in models, a very high recombination velocity is required to explain the data. Further modeling of the SOI data set using segregation of interstitials to the oxide would be very useful in determining whether the experimentally observed non-Gaussian diffusion profiles can be thus explained.
- FTIR studies of oxygen precipitation in Czochralski silicon under conditions similar to our buried layer experiments can lead to a better understanding of the bulk oxide precipitation and dissolution reactions that dominate.

Appendix A

Spreading Resistance Technique

The spreading resistance technique has been successfully used over the past two decades to determine one-dimensional vertical doping profiles in silicon. Extensive literature exists on this topic and will not be covered here. The purpose of this appendix is to acquaint the reader with techniques followed in this work to obtain diffusion coefficients from concentration profiles calculated from spreading resistance profiles.

Spreading resistance is a two-point comparative probe technique in which the probes travel down a bevelled sample as depicted in Figure A.1. A fixed voltage is applied between the probes and the current flowing between them, through the sample, is measured to yield the resistance of the sample in the area probed. Samples of known uniform resistivity are then measured on the same probe system and a calibration of resistance versus resistivity is obtained. Using this calibration in conjunction with SERAPES [23], an algorithm for converting resistance to concentration, the resistance of the unknown sample under consideration is then converted to a concentration (doping) profile.

However, since the current paths within the sample need not be restricted to the sample's surface, corrective factors are applied to obtain the surface resistance as closely as possible. The SERAPES algorithm that is used in this work considers a

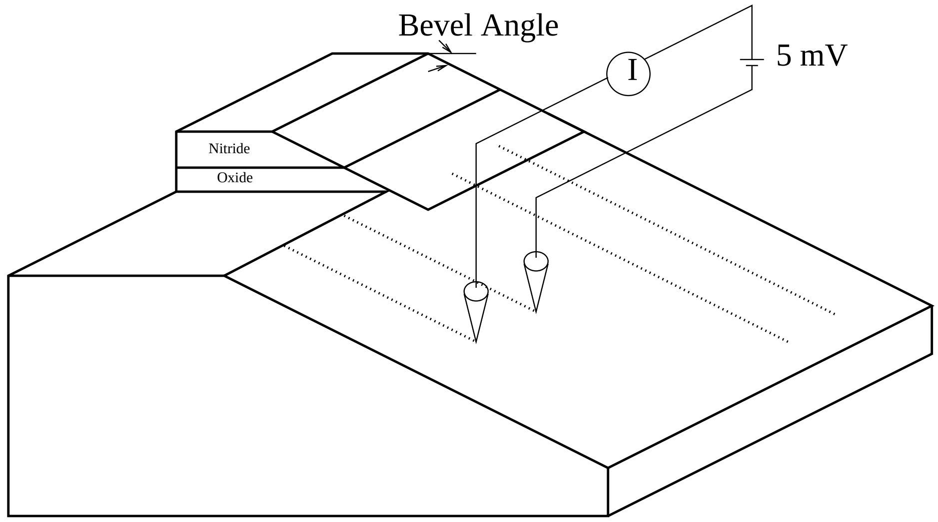

Figure A.1: *A schematic showing the spreading resistance technique*

barrier resistance model including carrier spilling and is of the form given by,

$$R = \rho \frac{CF}{2a} + A\rho^n. \tag{A.1}$$

Figure A.2 shows a flow diagram of the fitting procedure. SERAPES, a spreading resistance analysis program which includes the effects of carrier spilling [23], is used to calculate the doping profiles from the measured spreading resistance profiles. Measured starting and final resistance profiles are shown in Figure A.3. while Figure A.4 shows the converted concentration profiles. The calculated pre-oxidation sample doping profile is subsequently used as a starting profile for diffusion simulation via the process simulator SUPREM IV [52] and is compared to the calculated post-oxidation doping profiles in the inert and the oxidizing regions. profiles. In some cases the comparisons were made in the resistance domain. For this, the doping profiles resulting from the simulation were re-converted to resistance profiles (again using SERAPES) and compared to the measured post-oxidation spreading resistance profiles. A non-linear optimization program called PROFILE [66] selects an optimal diffusion coefficient for the given experimental conditions, via the process simula-

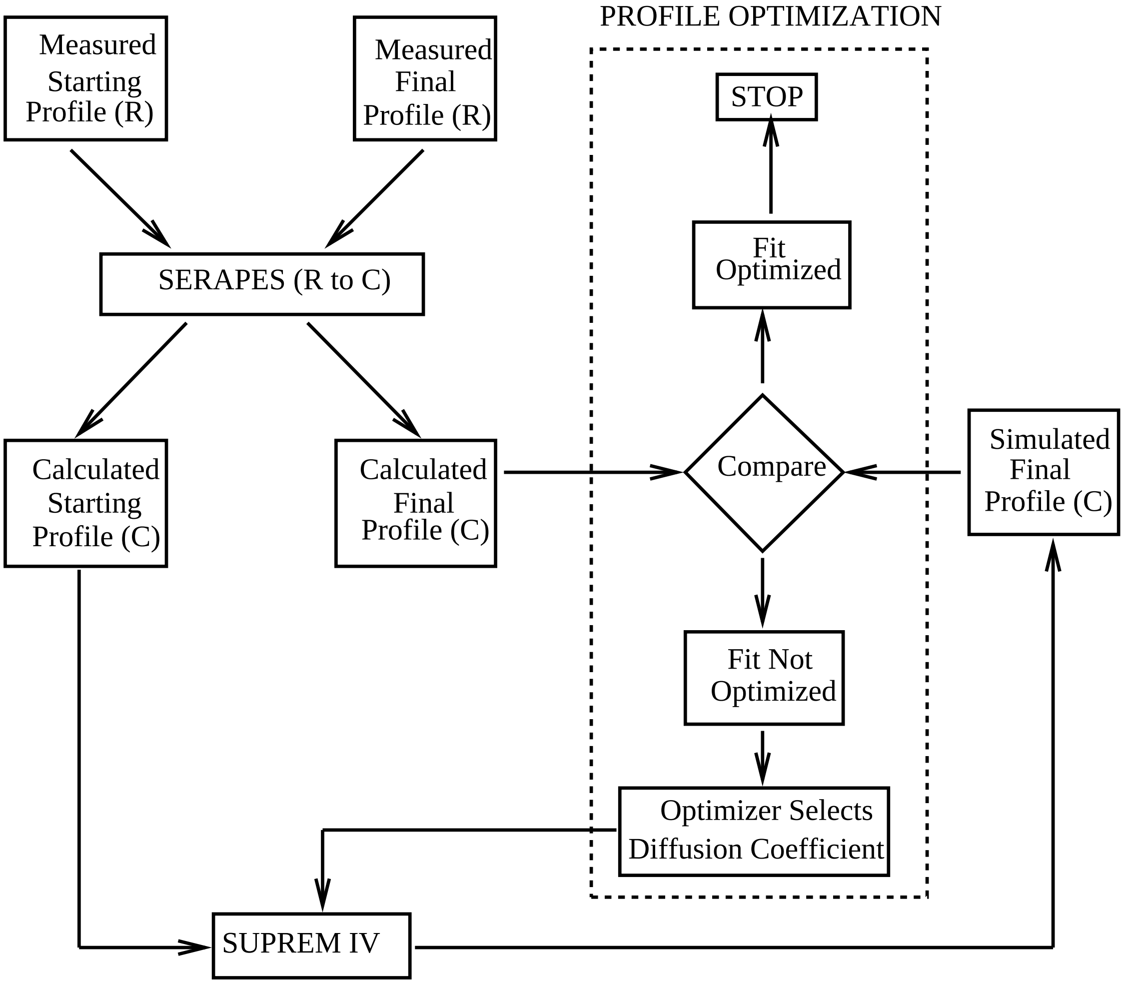

Figure A.2: *Flow diagram showing the general fitting procedure*

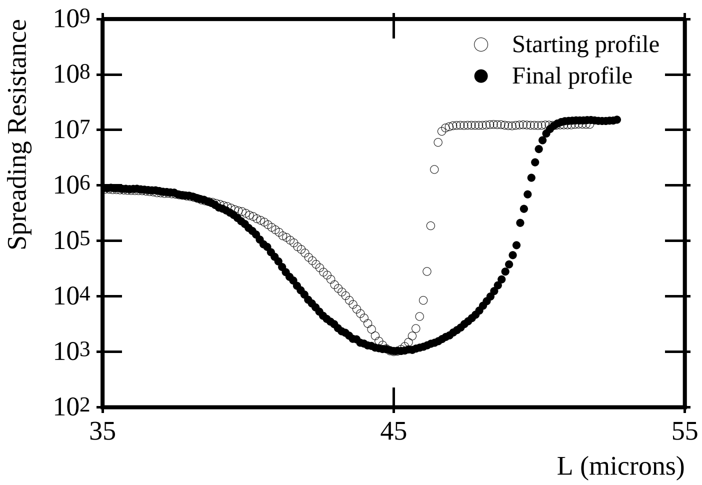

Figure A.3: *Typical spreading resistance initial and final profiles*

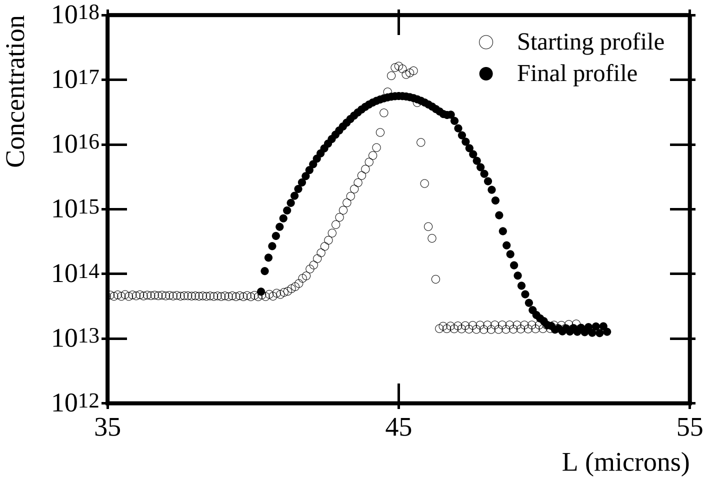

Figure A.4: *The initial and final spreading resistance profiles converted to the concentration domain using SERAPES*

tor SUPREM IV [52], till it obtains the best match between the starting and final concentration (or resistance) profiles.

The ratio of calculated phosphorus diffusivity in the region under investigation and that under inert conditions, D_P/D_P^*, is the supersaturation ratio. The error bars in all the figures are estimated error bounds on the calculated phosphorus diffusivity based on the accuracy of bevel angle measurements ($\pm1\%$) and variations between multiple profiles on single and multiple bevels.

Bibliography

[1] A. M. Agarwal and S. T. Dunham. Buried Layer Study: Bulk Interactions in Different Silicon Substrates. *unpublished.*

[2] A. M. Agarwal and S. T. Dunham. Determination of silicon point defect properties from oxidation enhanced diffusion of buried layers. *Appl. Phys. Lett.*, 63(6):800–802, 1993.

[3] S. T. Ahn. *Point defect mediated dopant diffusion in silicon.* PhD thesis, Stanford University, September 1988.

[4] S. T. Ahn, J. D. Shott, and W. A. Tiller. Determination of modeling parameters for silicon interstitial diffusion using silicon membranes. In *Proceedings, Electrochemical Society Meeting*, Oct 1986. San Diego, CA.

[5] G. B. Bronner and J. D. Plummer. *Mat. Res. Soc. Symp. Proc., Boston, MA*, 36:49, 1985.

[6] G. B. Bronner and J. D. Plummer. Gettering of gold in silicon: A tool for understanding the properties of silicon interstitials. *J.Appl. Phys.*, 61(12):5286, June 1987.

[7] G. K. Celler and L. E. Trimble. Catalytic effect of SiO on thermomigration of impurities in silicon-dioxide. *Appl. Phys. Lett.*, 54(15):1427, April 1989.

[8] C. L. Claeys, G. J. Declerck, and R. J. Van Overstraeten. The influence of annealing ambient on the shrinkage kinetics of oxidation-induced stacking faults in silicon. *Appl Phys. Lett.*, 35(10):797–799, 1979.

[9] S. Dannefaer. A systematic study of positron lifetimes in semiconductors. *J. Phys. C.: Solid St. Phys.*, 15:599, 1982.

[10] S. Dannefaer, G. W. Dean, D. P. Kerr, and B. G. Hogg. Influence of defects and temperature on the annihilation of positrons in neutron-irradiated silicon. *Phys. Rev. B.*, 14(7):2709, 1976.

[11] S. Dannefaer, N. Fruensgaard, S. K. Kupca, B. G. Hogg, and D. P. Kerr. A positron study of plastic deformation of silicon. *Can. J. of Phys*, 61:451, 1983.

[12] S. Dannefaer, B. Hogg, and D. Kerr. Positron annihilation in silicon at high temperatures. In L.C. Kimerling and J.M. Parsey, editors, *Proceedings, 13th Intl. Conf. on Defects in Semicond.*, pages 255–259, 1985.

[13] S. Dannefaer, D. P. Kerr, and B. G. Hogg. A study of defects in amorphous silicon films. *J. Appl. Phys.*, 54(1):155, 1983.

[14] S. Dannefaer, S. K. Kupca, B. G. Hogg, D.P. Kerr, and B.G. Hogg. Temperature dependence of the annihilation of positrons in Si containing divacancies and quadrivacancies. *Phys. Rev. B.*, 22(12):6135, 1980.

[15] M. J. Van Dort, H. Lifka, P. C. Zalm, R. C. M. de Kruif, W. B. de Boer, P. H. Woerlee, C. A. H. Juffermans, A. J. Walker, J. W. Slotboom, and N. E. B. Cowern. A high-resolution study of two-dimensional oxidation-enhanced diffusion in silicon. In *Tech Digest IEDM'93, Washington DC*, page 299, 1993.

[16] S. T. Dunham. In *Proceedings, Electrochemical Society, 89-9 Pennington, NJ*, 1989. Second Intl. Symp. on ULSI Science and Tech., edited by C.M. Osburn and J. Andrews.

[17] S. T. Dunham. Interstitial kinetics near oxidizing silicon interfaces. *J. Electrochem. Soc*, 136:250, 1989.

[18] S. T. Dunham. Interactions of silicon point defects with oxide films. *J. Appl. Phys.*, 71(2):685–696, 1992.

[19] S. T. Dunham, A. M. Agarwal, and N. Jeng. Determination of silicon point defect properties using buried layers and membranes. In *Proceedings, Electrochemical Society Meeting*, May 1990. Toronto, Canada.

[20] S. T. Dunham and B. Agrawal. Mater. Res. Soc. Proc. 105, Pittsburgh, PA, 1988. SiO2 and Its Interfaces, G. Lucovsky and S. Pantelides, eds.

[21] S. T. Dunham and J. D. Plummer. Point-defect generation during oxidation of silicon in dry oxygen-I. *J. Appl. Phys.*, 59(7):2541, April 1986.

[22] S. T. Dunham and J. D. Plummer. Point-defect generation during oxidation of silicon in dry oxygen-II. *J. Appl. Phys.*, 59(7):2551, April 1986.

[23] Scott T. Dunham, Nat Collins, and Nanseng Jeng. Improved analysis of spreading resistance measurements. *J. Vac. Sci. Technol. B*, 12(1):283–289, 1994.

[24] P. Fahey. *Point Defects and Dopant Diffusion in Silicon.* PhD thesis, 1985. Stanford Electronics Laboratory, Stanford University, Stanford, CA.

[25] P. Fahey, G. Barbuscia, M. Moslehi, and R. W. Dutton. Kinetics of thermal nitridation processes in the study of dopant diffusion mechanisms in silicon. *Appl. Phys. Let.*, 46:784, April 1985.

[26] P. Fahey and P. B. Griffin. Investigation of the mechanism of Si self-interstitial injection from nitridation of SiO2 films. *Semiconductor Silicon 1990*, 7:486–495, 1990.

[27] P. Fahey, P. B. Griffin, and J. D. Plummer. Point defects and dopant diffusion in silicon. *Reviews of Modern Physics*, 61(2):289–383, April,1989.

[28] R. B. Fair. Oxidation, impurity diffusion and defect growth in silicon - An overview. *J. Electrochem. Soc.*, 128:1360, 1981.

[29] M. Futagami and M. Hamazaki. Thermal etching of a (100) silicon surface. *Jpn. J. Appl. Phys.*, 21(12), 1982.

[30] C. Gelain, A. Cassuto, and P. Le Goff. Kinetics and mechanism of low-pressure, high-temperature oxidation of silicon-II. *Oxidation of metals*, 3(2):139–151, 1971.

[31] P. B. Griffin. *Physics and modeling of two-dimensional diffusion in SUPREM-IV*. PhD thesis, Stanford University, December 1989.

[32] P. B. Griffin, S. T. Ahn, W. A. Tiller, and J. D. Plummer. Model for bulk effects on Si interstitial diffusivity in silicon. *Appl. Phys. Let.*, 51(2):115, July 1987.

[33] P. B. Griffin, P. M. Fahey, J. D. Plummer, and R. W. Dutton. Measurement of silicon interstitial diffusivity. *Appl. Phys. Let.*, 47(3):319–321, August 1985.

[34] P. B. Griffin and J. D. Plummer. Point defect models for two dimensional diffusion kinetics. In *Proceedings, Electrochemical Society Meeting*, Oct 1986. San Diego, CA.

[35] P. B. Griffin and J. D. Plummer. Process physics determining 2-D impurity profiles in VLSI devices. *IEEE IEDM Tech. Dig.*, page 522, December, 7-10 1986.

[36] E. Guerrero, W. Jungling, H. Potzl, U. Gosele, M. Grasserbauer, L. Mader, and G. Stingeder. Determination of the retarded diffusion of antimony by SIMS measurements and numerical simulations. *J. Electrochem. Soc*, 133:2181, October 1986.

[37] J. Hirvonen and A. Antila. *Appl. Phys. Lett.*, 35:703, 1979.

[38] K. Hofmann and S. I. Raider. Acceleration factors for the decomposition of thermally grown SiO2 films. *J. Electrochem. Soc.*, 134(1):240–244, 1987.

[39] K. Hofmann, G. W. Rubloff, M. Liehr, and D. R. Young. High temperature reaction and defect chemistry at the Si/SiO2 interface. *Applied Surface Science*, 30:25–31, 1987.

[40] K. Hofmann, G. W. Rubloff, and R. A. McCorkle. Defect formation in thermal SiO2 by high-temperature annealing. *Appl. Phys. Lett.*, 49(22):1525–1527, 1986.

[41] M. A. Hopper, R. A. Clarke, and L. Young. Thermal oxidation of silicon: In situ measurement of the growth rate using ellipsometry. *J. Electrochem. Soc.*, 122(9):1216–1222, 1975.

[42] M. A. Hopper, R. A. Clarke, and L. Young. Removal of oxide films from silicon surfaces in a high vacuum system: An in-situ ellipsometric study. *Surface Science*, 56:472–481, 1976.

[43] S. M. Hu. Formation of stacking faults and enhanced diffusion in the oxidation of silicon. *J. Appl. Phys.*, 45(4):1567, April 1974.

[44] S. M. Hu. *Defects in Semiconductors*. North Holland, New York, 1981.

[45] A. Ishizaka and Y. Shiraki. Low temperature surface cleaning of silicon and its application to silicon MBE. *J. Electrochem. Soc.*, 133(4):667, 1986.

[46] Nanseng Jeng. Enhanced phosphorus diffusion during thermal oxidation of silicon. Master's thesis, Boston University, 1991.

[47] L. Kalinowski and R. Seguin. *Appl Phys. Lett.*, 35:211, 1979.

[48] H. W. Kennel and J. D. Plummer. In *Proceedings, Electrochemical Society Meeting*, May 1990. Toronto, Canada.

[49] Harold W. Kennel. *Physical Modeling Of Oxygen Precipitation, Defect Formation and Diffusion In Silicon*. PhD thesis, Stanford University, February 1991.

[50] S. Kordic, E. J. van Loenen, and Andrew J. Walker. Two-dimensional imaging of cleaved Si p-n junctions with 30-nm resolution using a UHV scanning tunneling microscope. *IEEE Electon Device Letters*, 12(8):422, 1991.

[51] M. Lannoo and J. Bourgoin. *Point Defects in Semiconductors, Theoretical Aspects*. Springer Series in Solid-State Sciences, No. 22. Springer, New York, 1981.

[52] M. E. Law and R. W. Dutton. *IEEE Trans. Comp. Aid. Des.*, 7:181, 1988.

[53] M. Liehr, G. B. Bronner, and J. E. Lewis. Stacking-fault-induced defect creation in SiO2 on Si(100). *Appl Phys. Lett.*, 52(22):1892–1894, 1988.

[54] M. Liehr, J. E. Lewis, and G. W. Rubloff. Kinetics of high-temperature thermal decomposition of SiO2 on Si(100). *J. Vac. Sci. Technol. A*, 5(4):1559–1562, 1987.

[55] V. G. Lifshits, I. G. Kaverina, V. V Korobtsov, A. A Saranin, and A. V. Zotov. Thermal annealing behaviour of Si/SiO2 structures. *Thin Solid Films*, 135:99–105, 1986.

[56] A. M. Lin, R. W. Dutton D. Antoniadis, and W. A. Tiller. The growth of oxidation stacking faults and the point defect generation at Si-SiO interface during thermal oxidation of silicon. *J. Electrochem. Soc.*, 128(5):1121, May 1981.

[57] A. M. Lin, R. W. Dutton, and D. A. Antoniadis. The lateral effect of oxidation on boron diffusion in <100> silicon. *Appl. Phys. Lett.*, 35(10):799, November 1979.

[58] S. Mantovani, F. Nava, C. Nobili, and G. Ottaviani. In-diffusion of Pt in Si from the PtSi/Si interface. *Phys. Rev. B*, 33(8):5536, April 1986.

[59] J. P. Meindl, R. W. Dutton, K. C. Saraswat, J. D. Plummer, T. I. Kamins, and B. E. Deal. chapter Process and Device Modeling for Integrated Circuit Design. Noordhoff, Leyden, 1977. Silicon Epitaxy and Oxidation, F. Van de Wiele, W. L. Engl and P.O. Jespers, eds.

[60] S. Mizuo and H. Higuchi. Retardation of Sb diffusion in Si during thermal oxidation. *Jap. J. Appl. Phys.*, 20(4):739, April 1981.

[61] S. Mizuo and H. Higuchi. Anomalous diffusion of B and P in Si directly masked with silicon-nitride. *Jap. J. Appl. Phys.*, 21(2):281, February 1982.

[62] S. Mizuo and H. Higuchi. The range of diffusion enhancement of B and P in Si during thermal oxidation. *Jap. J. Appl. Phys.*, 21(2):272, February 1982.

[63] S. Mizuo, T. Kusaka, A. Shintani, M. Nanba, and H. Higuchi. Effect of Si and SiO2 thermal nitridation on impurity diffusion and oxidation induced stacking fault size in Si. *J. Appl. Phys.*, 54(7):3860, July 1983.

[64] F. Montillo and P. Balk. High-temperature annealing of oxidized silicon surfaces. *J. Electrochem. Soc.*, 118(9):1463–1468, 1971.

[65] F. F. Morehead, N. A. Stolwijk, Meyberg, and U. Gosele. Self-interstitial and vacancy contributions to silicon self-diffusion determined from the diffusion of gold in silicon. *Appl. Phys. Lett.*, 42(8):690, April 1983.

[66] G. J. L. Ouwerling, F. van Rijs, H. M. Wentinck, J. C. Staalenburg, and W. Crans. Physical parameter extraction by inverse modelling of semiconductor devices. In *Proceedings of the third conference on Simulation of Semiconductor Devices and Processes (SISDEP-88)*, pages 599–610, September 1988. G. Baccarani and M. Rudan, eds., (Alma Mater Studiorum Saecularia, Bologna, Italy).

[67] Paul A. Packan. *Physical Modeling Of Transient Diffusion Effects In Silicon Due to Surface Oxidation And Ion-Implantation.* PhD thesis, Stanford University, February 1991.

[68] A. Reisman, S. T. Edwards, and P. L. Smith. On the thermal etching of silicon. *J. Electrochem. Soc.*, 135(11):2848–2858, 1988.

[69] A. Reisman and D. Temple. Differences in Surface Erosion of Silicon Wafers Annealed in Si-Loaded, SiC-Coated and Pure SiC Carriers. *J. Electrochem. Soc.*, 138(5):L1, 1991.

[70] A. Reisman, D. Temple, and P. L. Smith. Further comments on the thermal etching of silicon. *J. Electrochem. Soc.*, 137(1):284–290, 1990.

[71] W. B. Rogers and H. Z. Massoud. Determination of the Kinetic Coefficients of Silicon Self-Interstitials from Oxygen Precipitation/Front-Surface Stacking-Fault Growth Experiments. volume 138, page 3492, 1991.

[72] W. B. Rogers and H. Z. Massoud. Determination of the Kinetic Coefficients of Silicon Self-Interstitials from Back-Side Oxidation/Front-Surface Stacking-Fault Growth Experiments. *J. Electrochem. Soc.*, 138(11):3483, 1991.

[73] G. W. Rubloff, K. Hofmann, M. Liehr, and D. R. Young. Defect microchemistry at the SiO2/Si interface. *Phys. Rev. Lett.*, 58(22):2379–2382, 1987.

[74] G. W. Rubloff, R. M. Tromp, E. J. van Loenen, P. Balk, and F. K. LeGoues. *J. Vac. Sci. Technol. A*, 4(3):1024, 1986.

[75] E. Scheid and P. Chenevier. 1D simulation of oxidation-enhanced and oxidation-retarded diffusion in silicon and validity of the physical model. *Phys. Stat. Solidi*, 93:523, 1986.

[76] Y. Shibata, S. Hashimoto, K. Taniguchi, and C. Hamaguchi. Oxidation enhanced diffusion of phosphorus over a wide range of oxidation rates. *J. Electrochem. Soc.*, 139(1):231–237, 1992.

[77] E. Sirtl, 1977. H. R. Huff and E. Sirtl, eds.

[78] N. A. Stolwijk, B. Schuster, and J. Holzl. Diffusion of gold in silicon studied by means of neutron-activation analysis and spreading resistance measurements. *Appl. Phys. A*, 33:133–140, 1984.

[79] R. A. Swalin. *Thermodynamics of Solids*. Wiley, New York, 1972.

[80] S. Miyazawa T. Yonehara, S. Yoshioka. Competing processes of Si molecular beam reactive etching and simultaneous deposition on film and bulk oxide. *J. Appl. Phys.*, 53(10):6839–6842, 1982.

[81] Michiharu Tabe. Etching of oxide films by Si in UHV. *Jpn. J. Appl. Phys.*, 21(3):534–538, 1982.

[82] T. Y. Tan and U. Gosele. Growth kinetics of oxidation induced stacking faults in silicon: A new concept. *Appl. Phys. Lett.*, 39(1):86, July 1981.

[83] T. Y. Tan and U. Gosele. Point defects, diffusion processes, and swirl defect formation in silicon. *Appl. Phys. A*, 37:1, 1985.

[84] T. Y. Tan and C. Y. Kung. Oxygen precipitation retardation and recovery phenomena in Czochralski silicon: Experimental observations, nuclei dissolution model, and relevancy with nucleation issues. *J. Appl. Phys.*, 59:917, 1986.

[85] K. Taniguchi and D. A. Antoniadis. Kinetics of self-interstitials generated at the Si/SiO2 interface. *Appl. Phys. Let.*, 42(11):961, 1983.

[86] K. Taniguchi and D. A. Antoniadis. Lateral extent of oxidation-enhanced diffusion of phosphorus in (100) silicon. *Appl. Phys. Let.*, 46(10):944, 1985.

[87] K. Taniguchi, Y. Shibata, and C. Hamaguchi. Theoretical model for self interstitial generation at the Si/SiO2 interface during thermal oxidation of silicon. *J. Appl. Phys*, 65:2723, 1989.

[88] D. J. D. Thomas. *Phys. Status Solidi*, 3:2261, 1963.

[89] W. A. Tiller. On the kinetics of the thermal oxidation of silicon - Coupling with other key phenomena. *J. Electrochem. Soc.*, 128:689, 1980.

[90] W. A. Tiller. *J. Appl. Phys.*, 64:375, 1987.

[91] R. Tromp, G. W. Rubloff, P. Balk, and F. K. LeGoues. High-temperature SiO2 decomposition at the SiO2/Si interface. *Phys. Rev. Lett.*, 55(21):2332–2335, 1985.

[92] G. D. Watkins. EPR studies of the lattice vacancy and low-temperature damage processes in silicon. In *Lattice Defects in Semiconductors,1974*, pages 1–21, 1975. F. A. Huntley, ed., Inst. Phys. Conf. Ser. No. 23, Institute of Physics, London.

[93] G. N. Willis. *Solid-State Electronics*, 12:133, 1969.